SOME FACTORS INFLUENCING
THE STRESS-STRAIN BEHAVIOUR OF CLAYS

by

A.S.BALASUBRAMANIAM

VOLUME II

Figures
Chapters I to 4

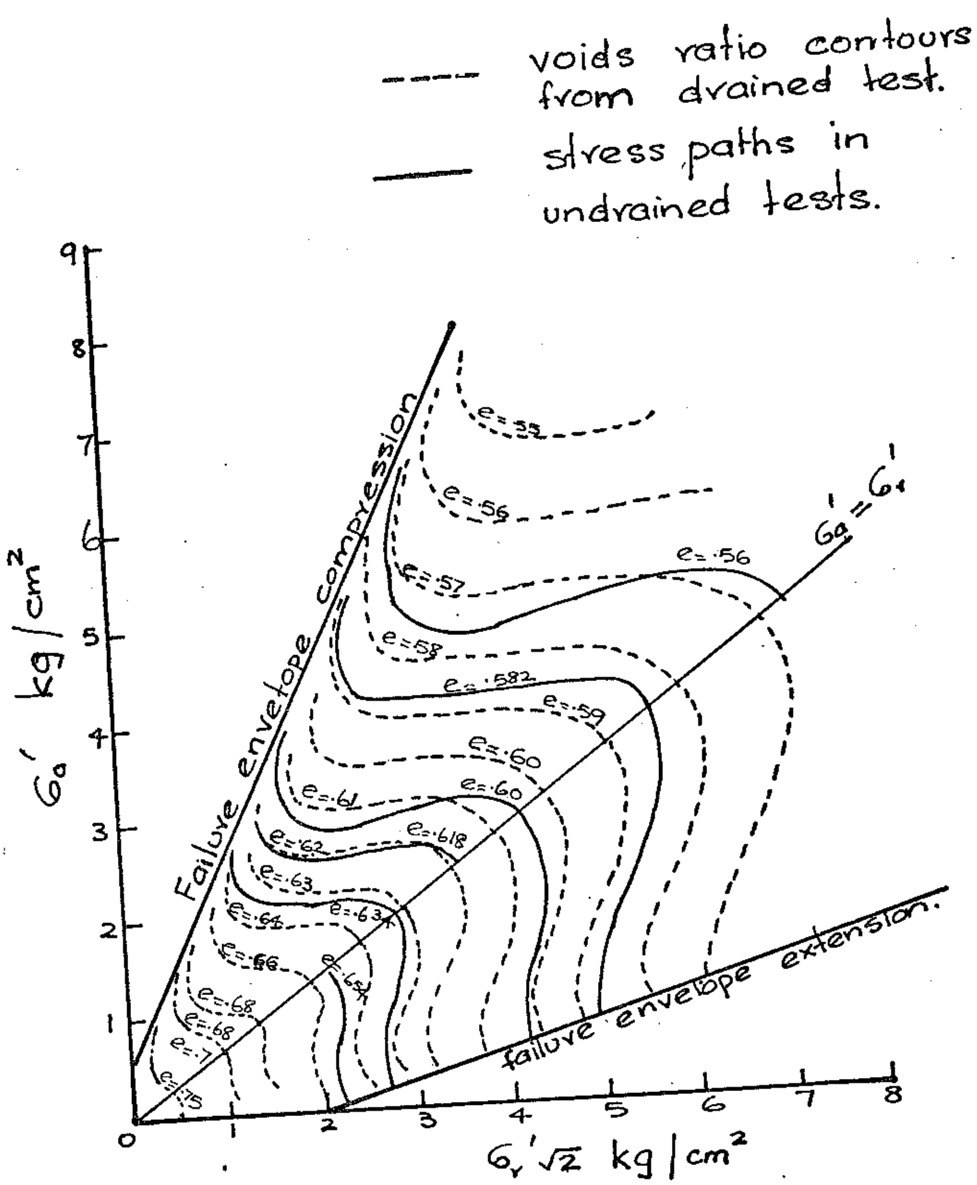

Fig. 1.1 Constant voids ratio contours of Rendulic (1936b, 1937). Quoted from Henkel (1960)

1 - σ_a' increased, σ_r' constant.

2. - σ_a' constant σ_r' increased

3. - $(\sigma_a' + 2\sigma_r')$ constant.

4. - σ_a' decreased, σ_r' constant.

5. - σ_a' constant, σ_r' decreased.

6. - $(\sigma_a' + 2\sigma_r')$ constant.

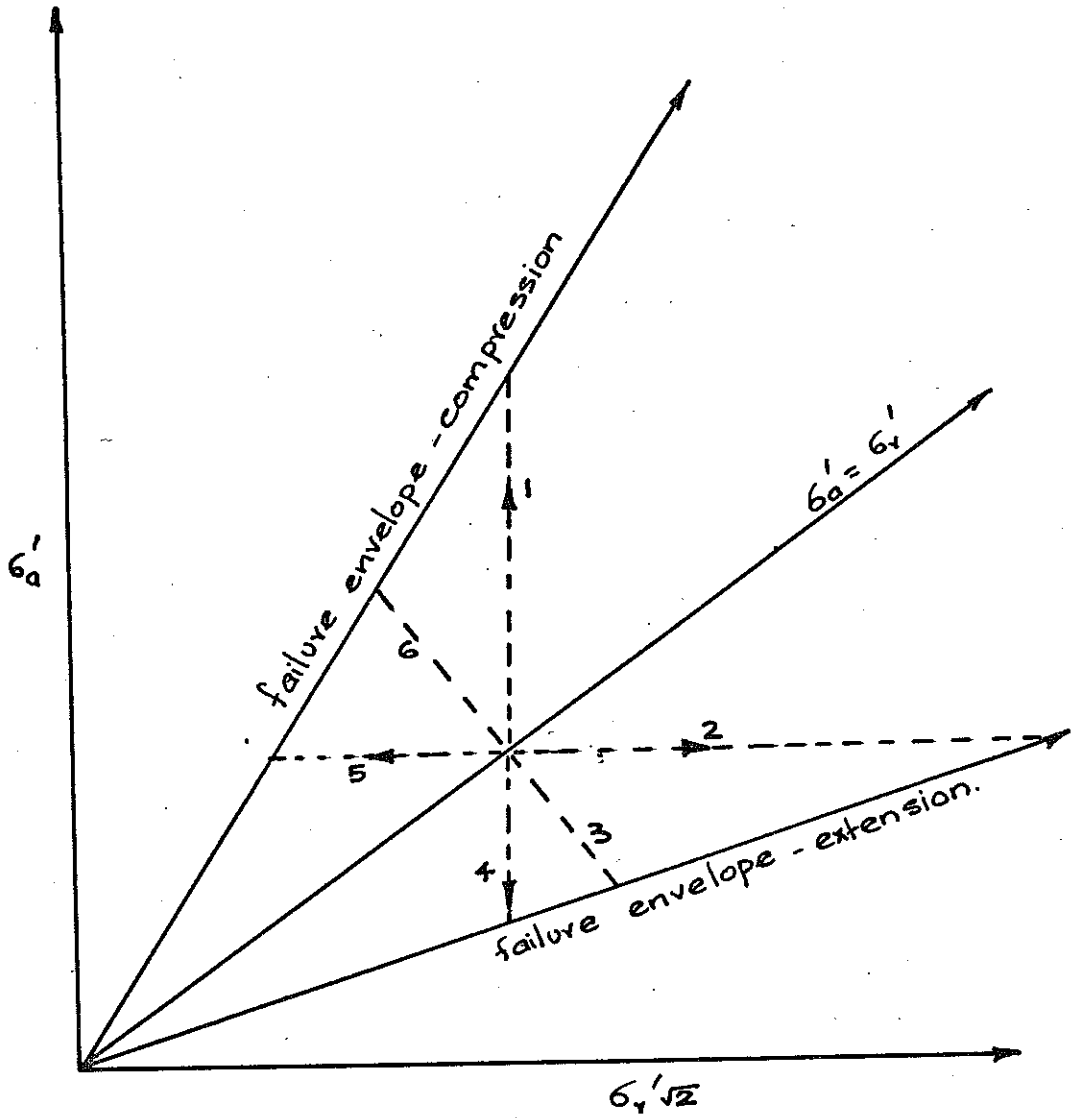

Fig. 1.2 (a) Stress paths of specimens in drained tests. (after Henkel (1960))

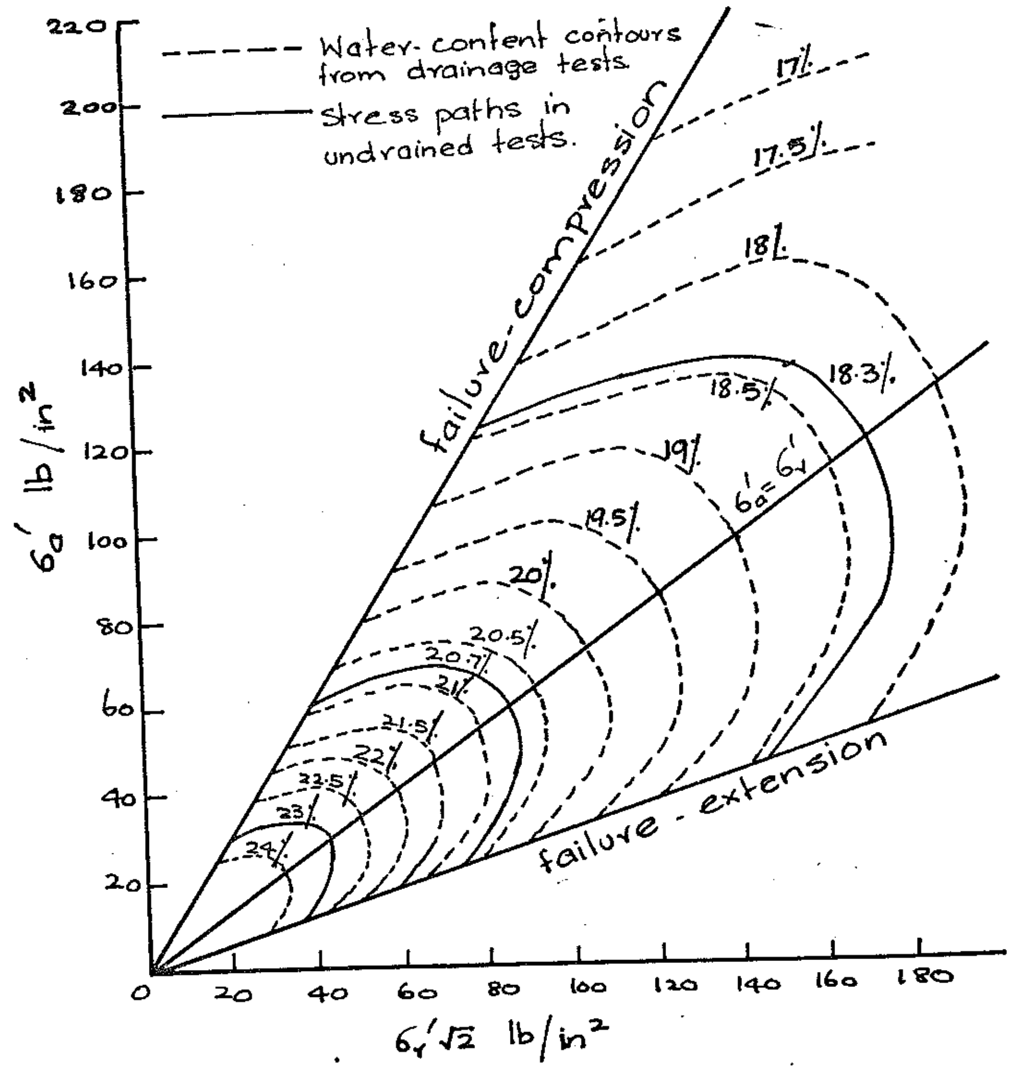

Fig. 1.2 (b). Water content contours from drained tests and stress paths in undrained test for normally consolidated specimens of Weald clay (after Henkel (1960))

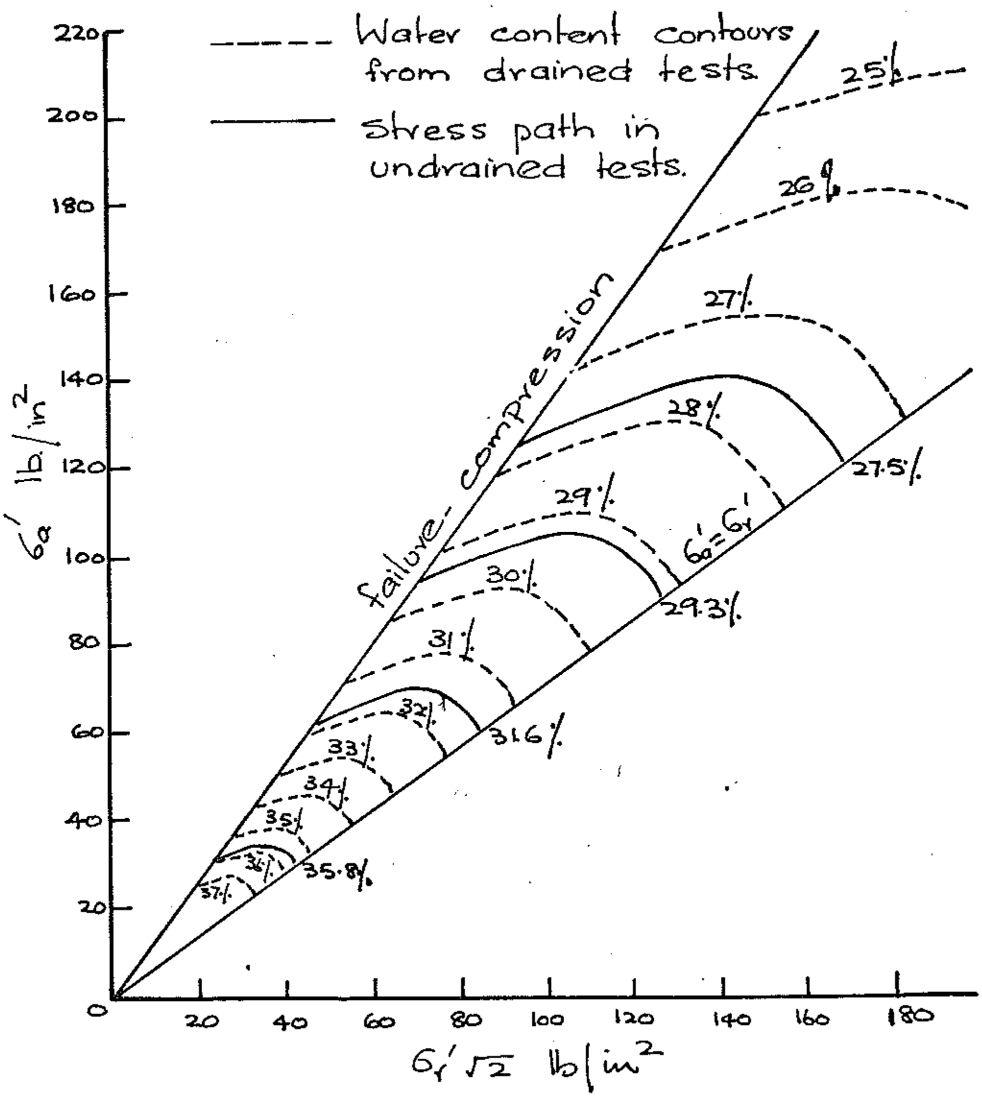

Fig. 1.2 (c) Constant water content contours from drained tests and undrained stress paths for normally consolidated specimens of London clay.

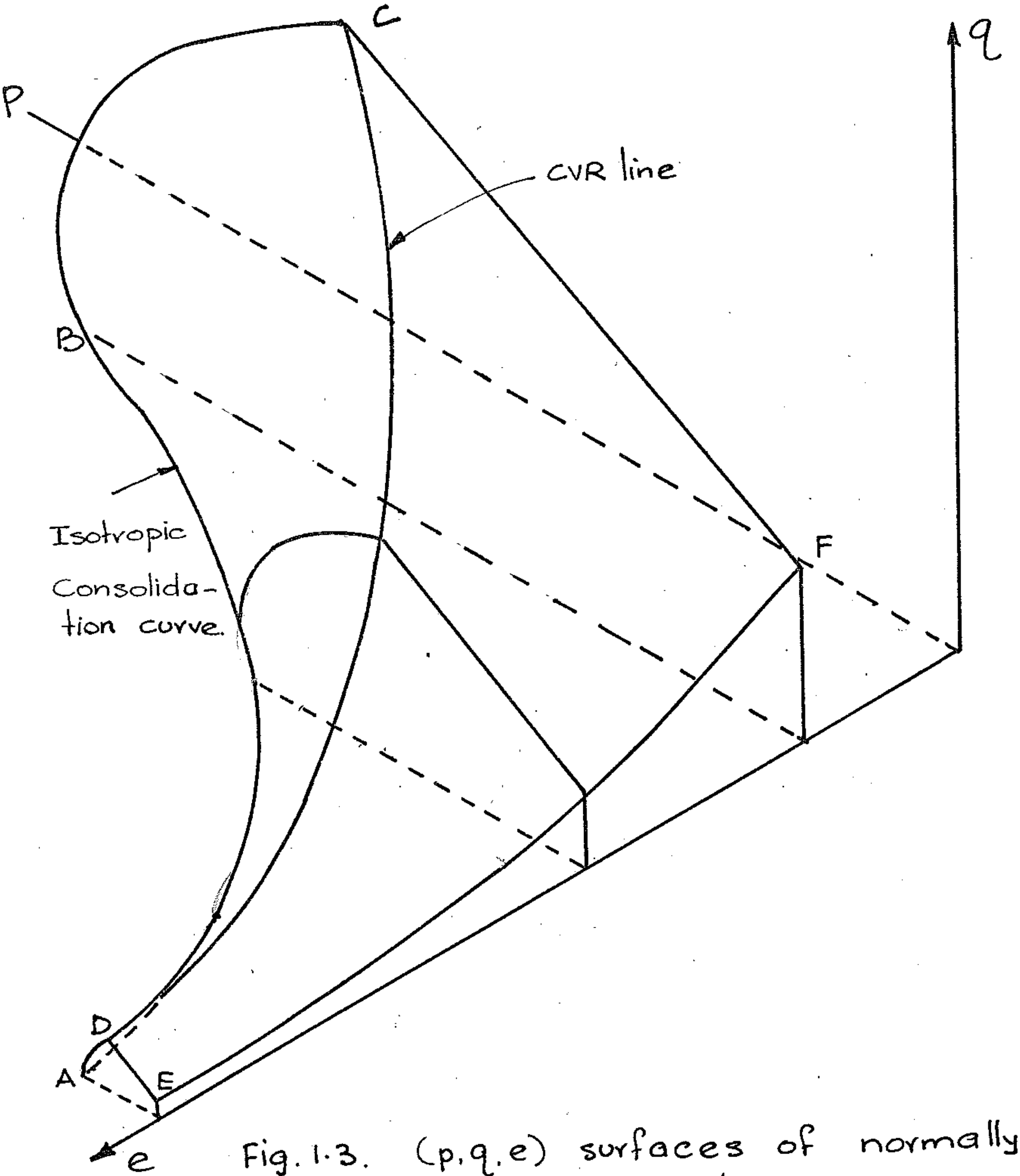

Fig. 1.3. (p, q, e) surfaces of normally and overconsolidated clay specimens. (after Roscoe, Schofield and Wroth (1958))

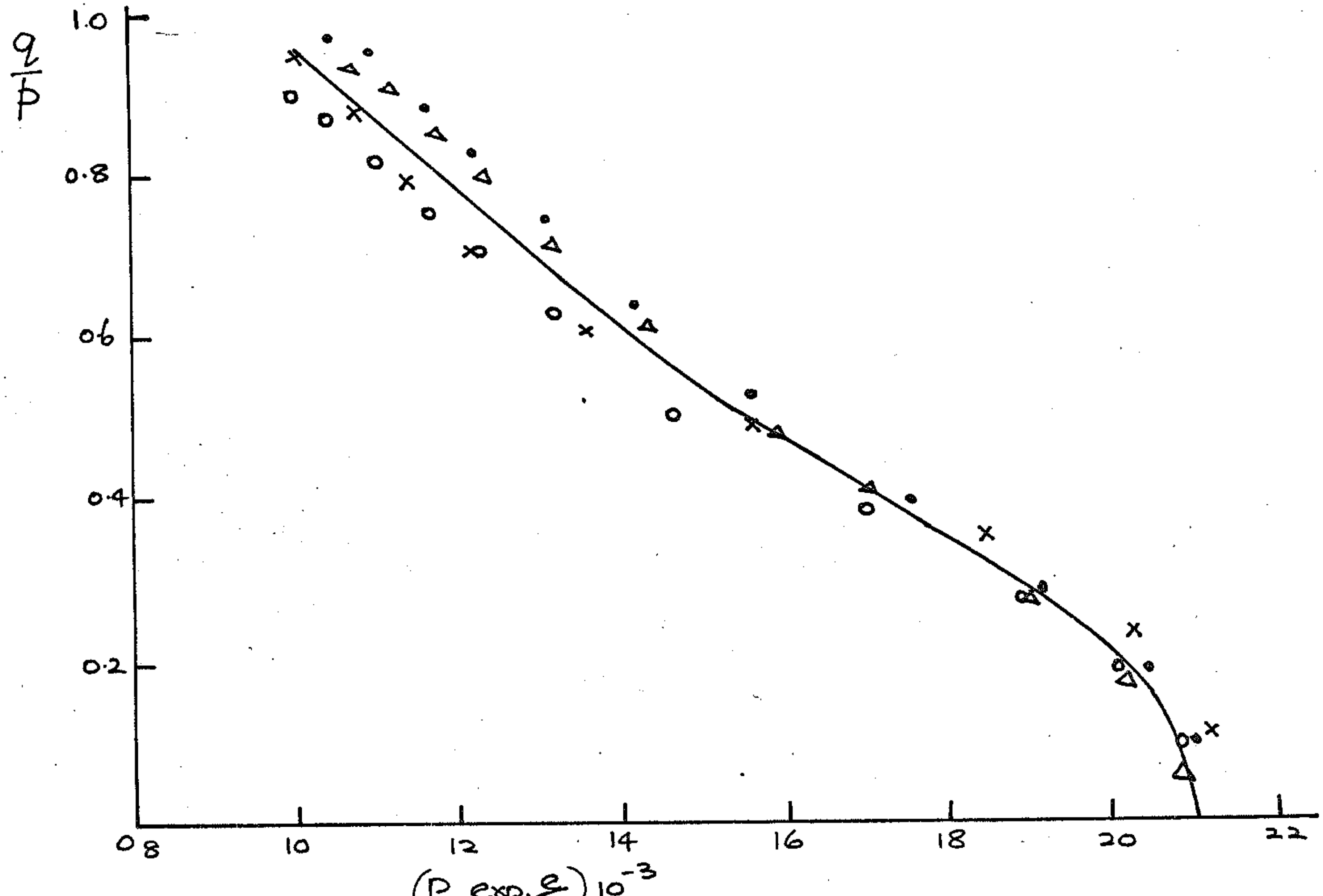

Fig. 1.4 (a). The q/p, $(p \exp. e/\lambda)\,10^{-3}$ characteristics for undrained triaxial compression tests on Kaolin.
(afte Roscoe - Thurairajah (1964))

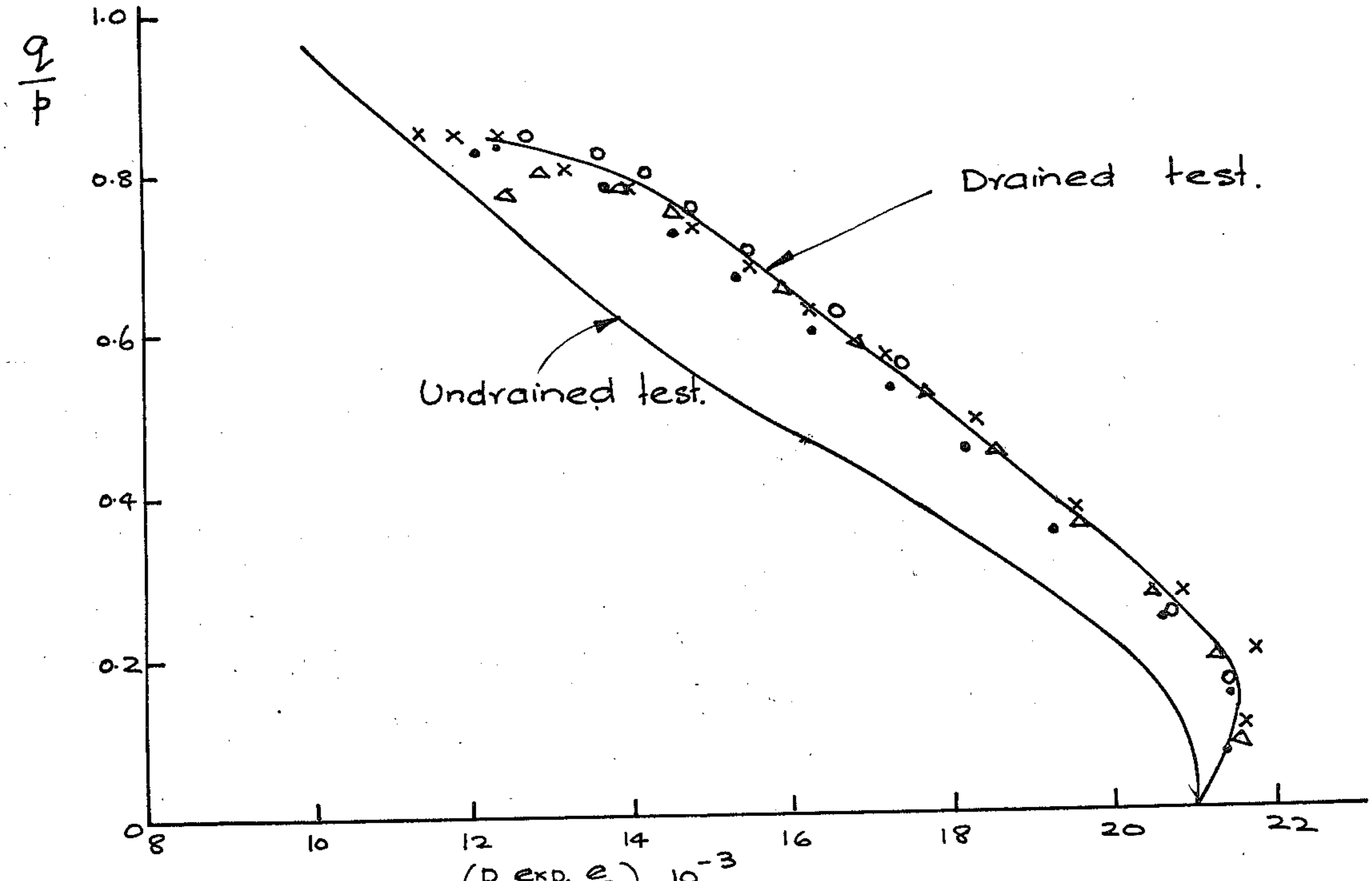

Fig. 1.4(b) The q/p, $(p \exp. \frac{e}{\lambda})10^{-3}$ characteristics for drained and undrained triaxial compression tests on Kaolin (after Roscoe and Thurairajah (1964))

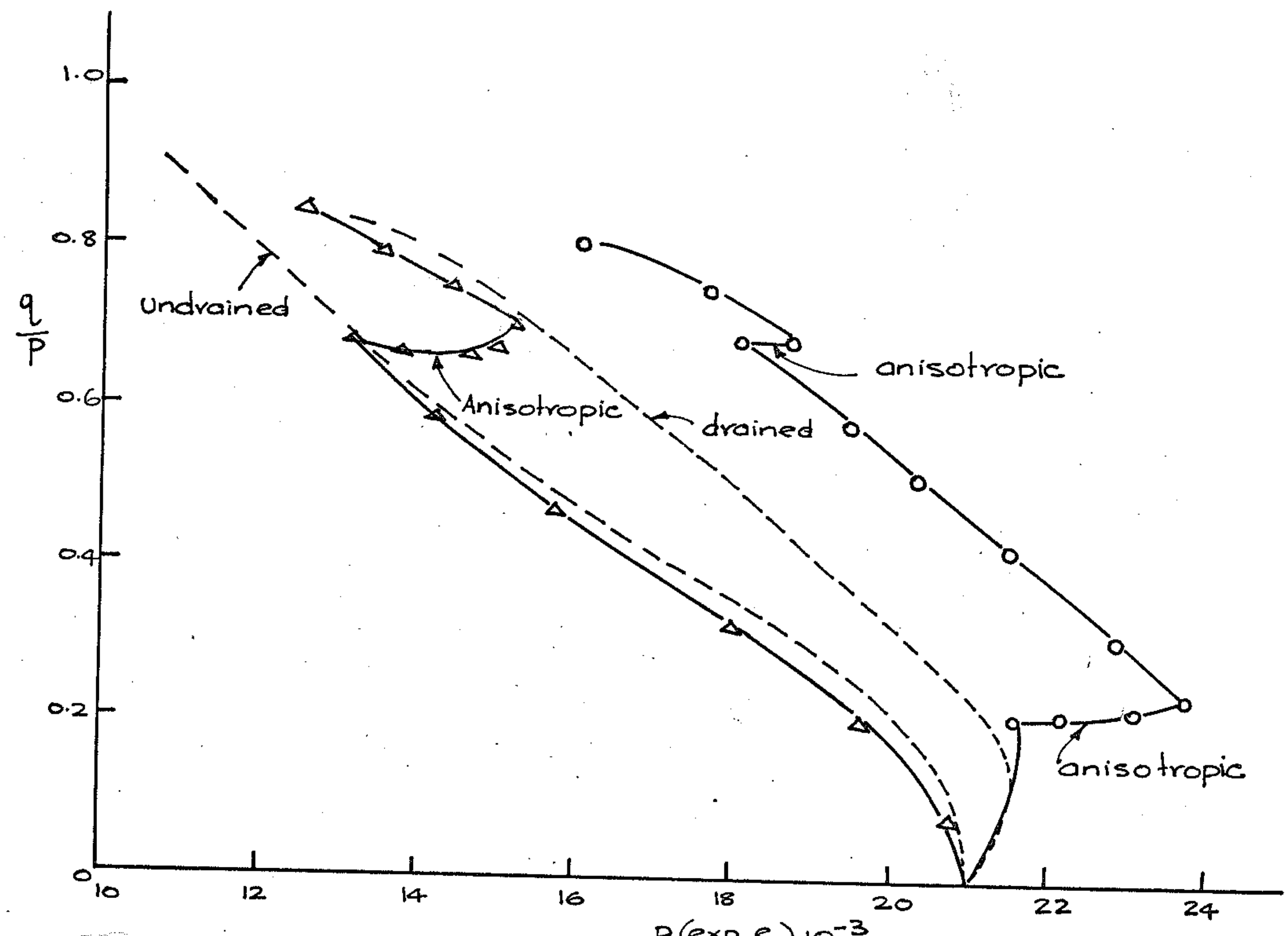

Fig. 1.4(c) Anisotropic consolidation paths in the $\left(\frac{q}{p},\ p(\exp.\frac{e}{\lambda})10^{-3}\right)$ plot.

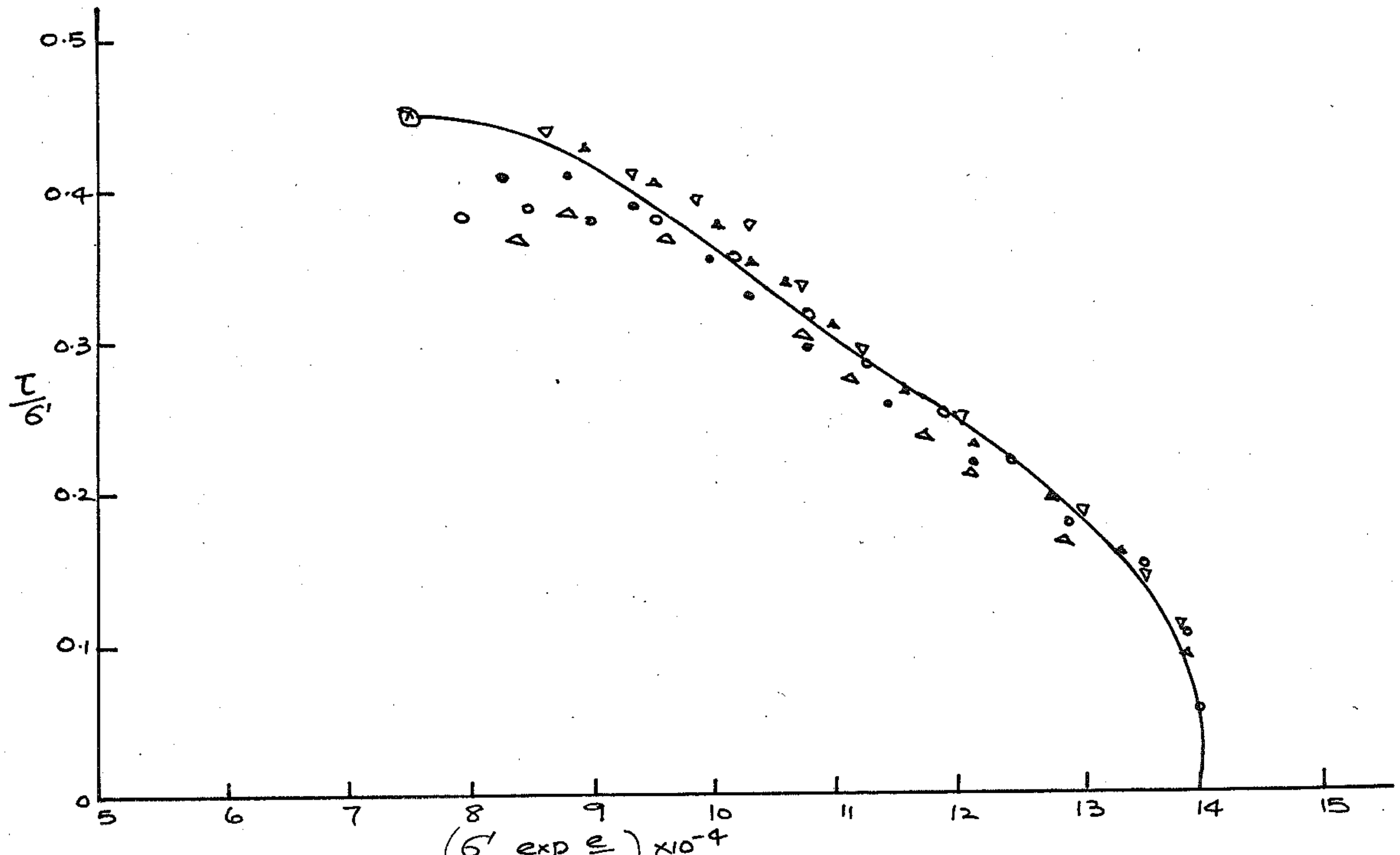

Fig. 1.5(a). The $\frac{\tau}{\sigma'}$, $(\sigma' \exp. e/\lambda) 10^{-4}$ characteristics for undrained tests on Kaolin in S.S.A.
(after Roscoe and Thurairajah (1964))

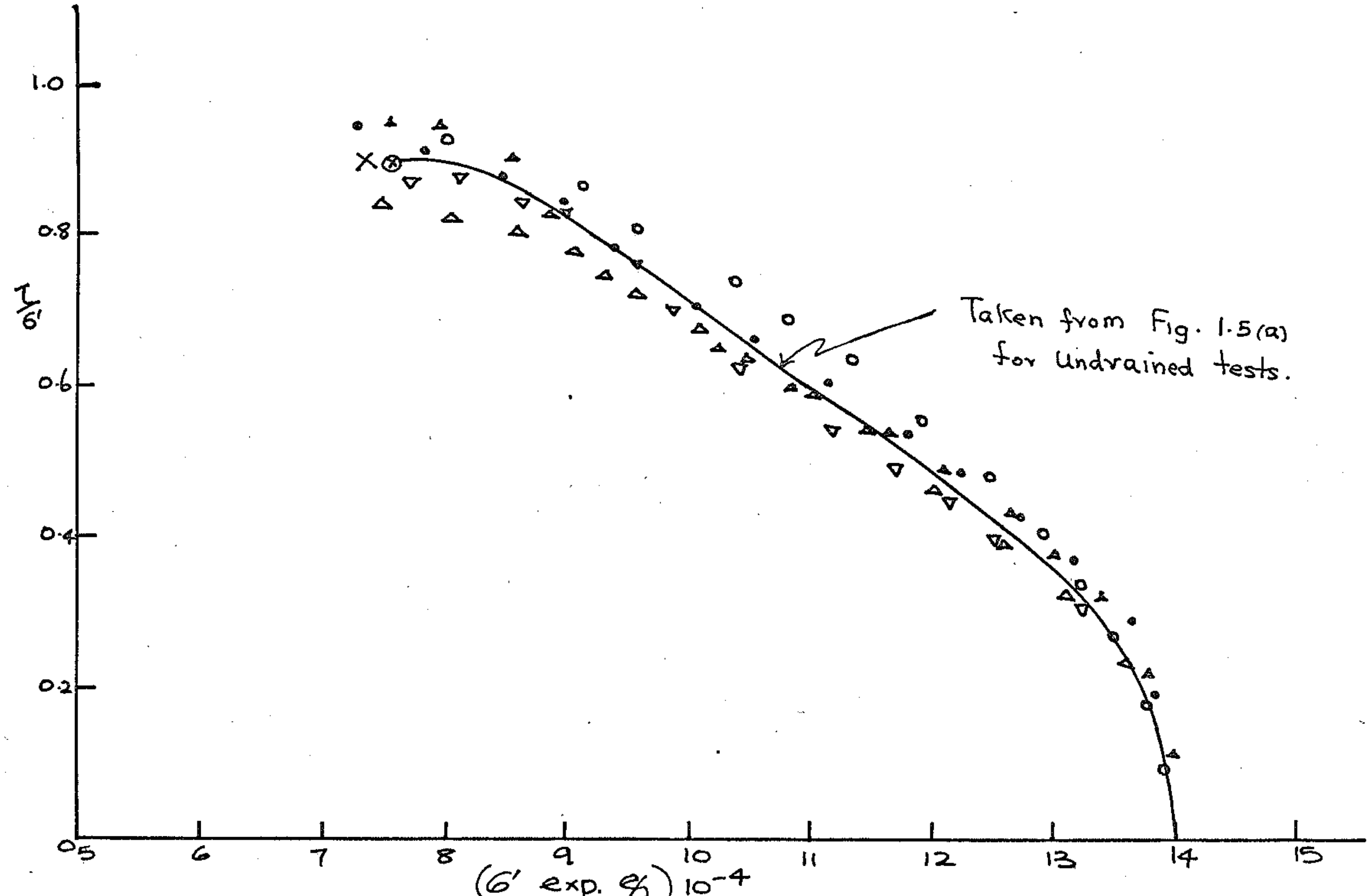

Fig. 1.5(b) Comparison of undrained and drained τ/σ', $(\sigma' \exp. e/\lambda)10^{-4}$ characteristics for Kaolin in S.S.A. (after Roscoe and Thuvairajah (1964))

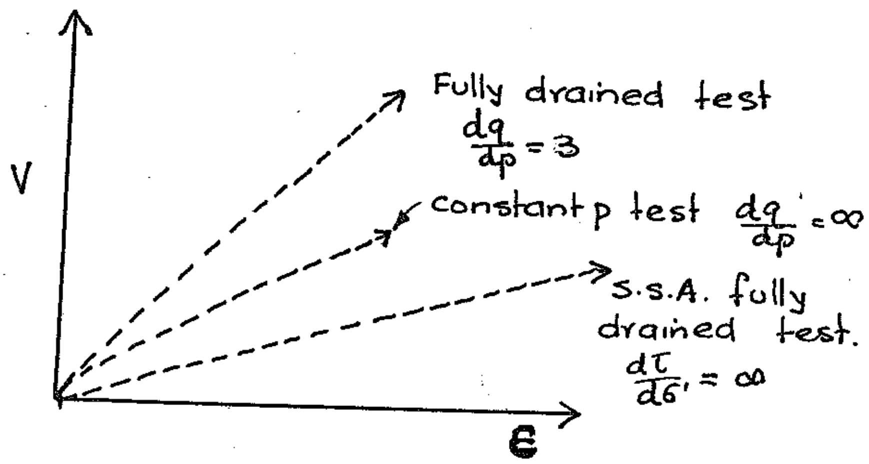

Fig. 1.6 The strain paths followed by specimens in the triaxial apparatus and S.S.A.

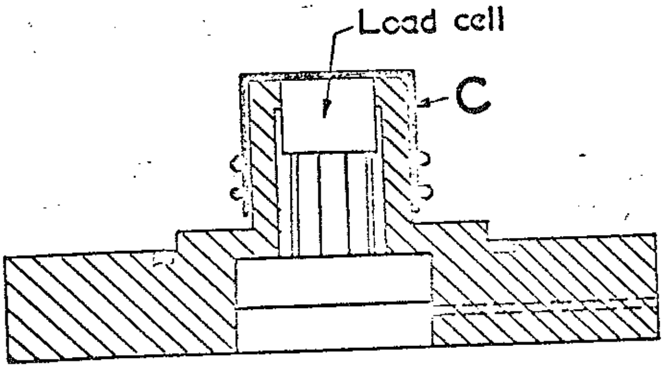

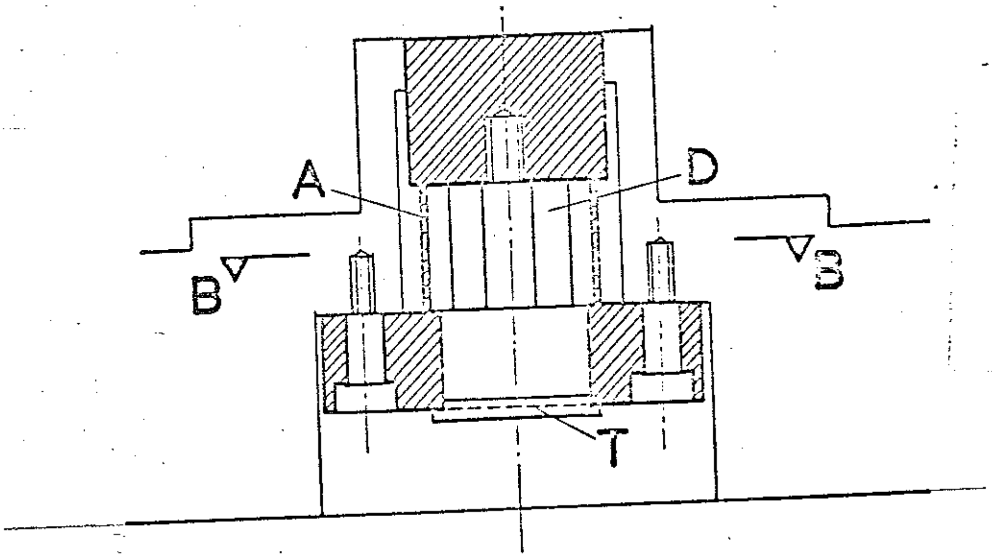

Sectional Elevation

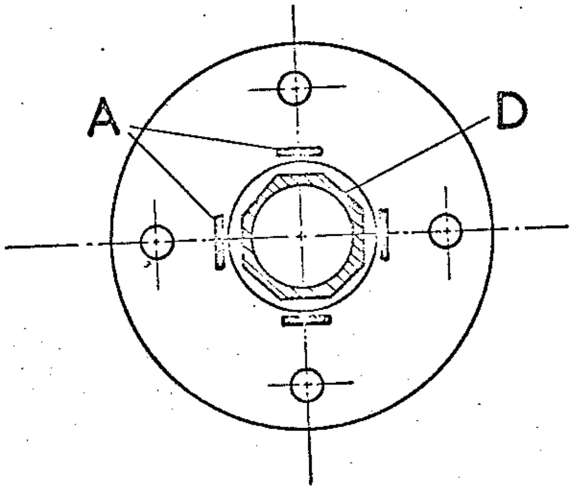

Section B-B

FIG.2.1 LOAD CELL USED IN CONSOLIDOMETERS

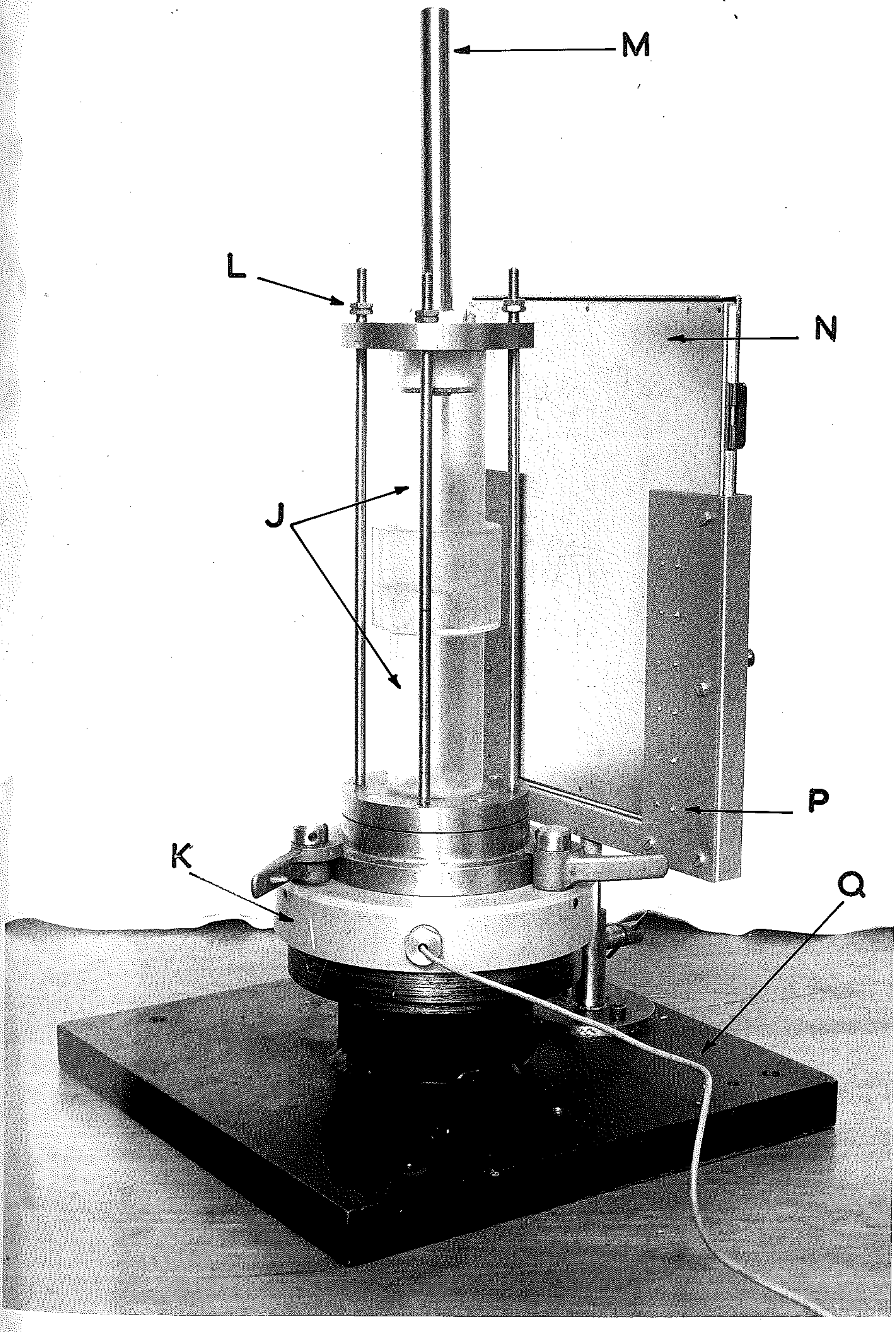

FIG.2.2 PERSPEX CONSOLIDOMETER

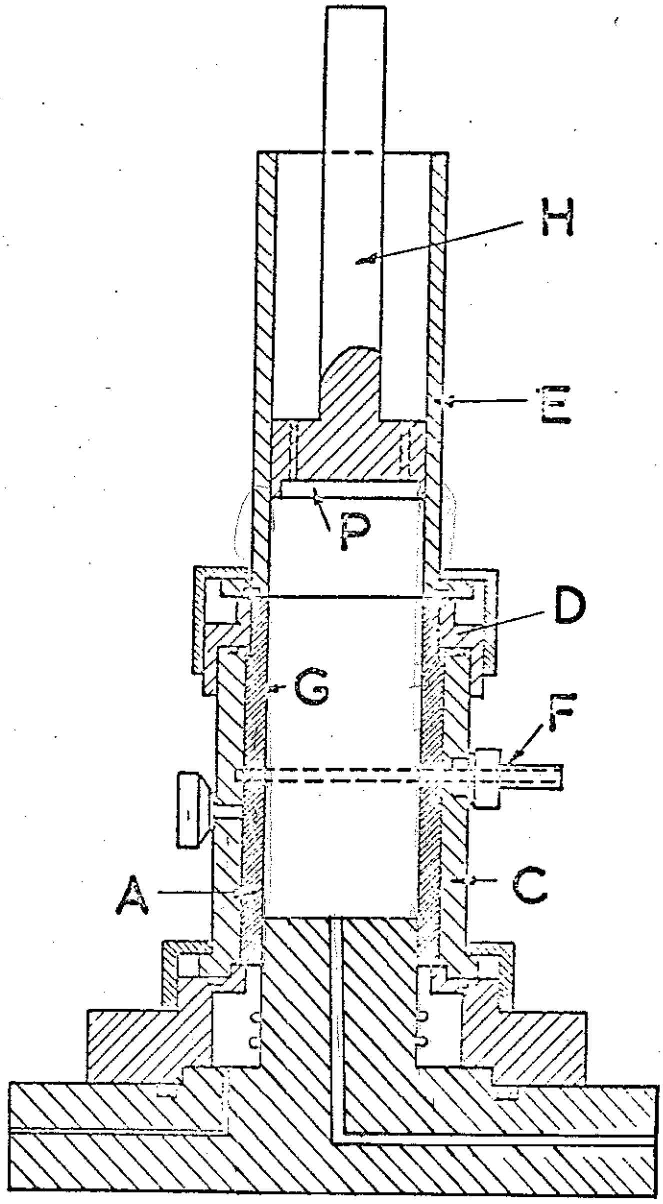

FIG.2.3 SAMPLE FORMER FOR TRIAXIAL SPECIMENS

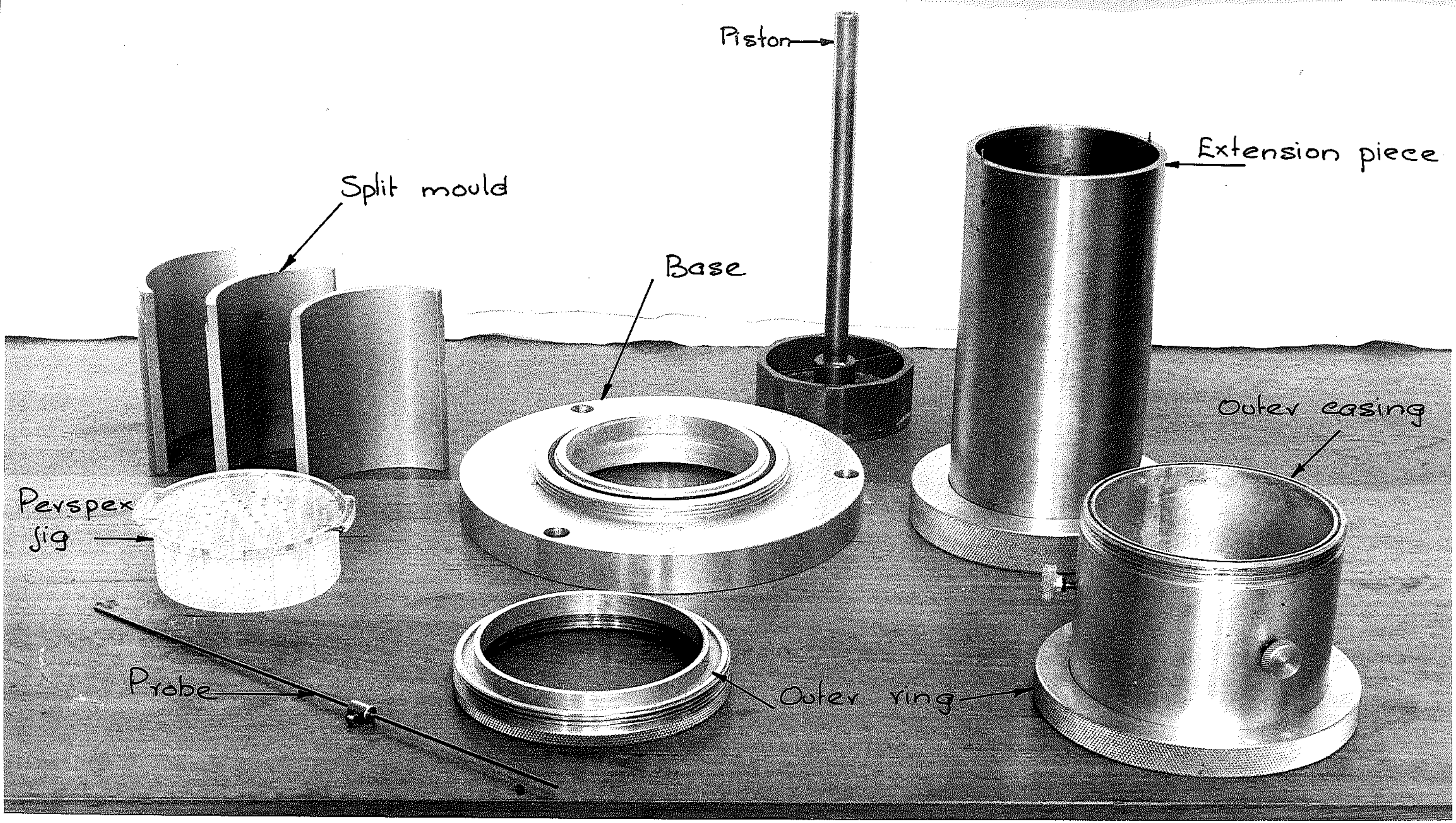

FIG. 2.4 TRIAXIAL FORMER FOR 4 INCH DIAMETER SAMPLE

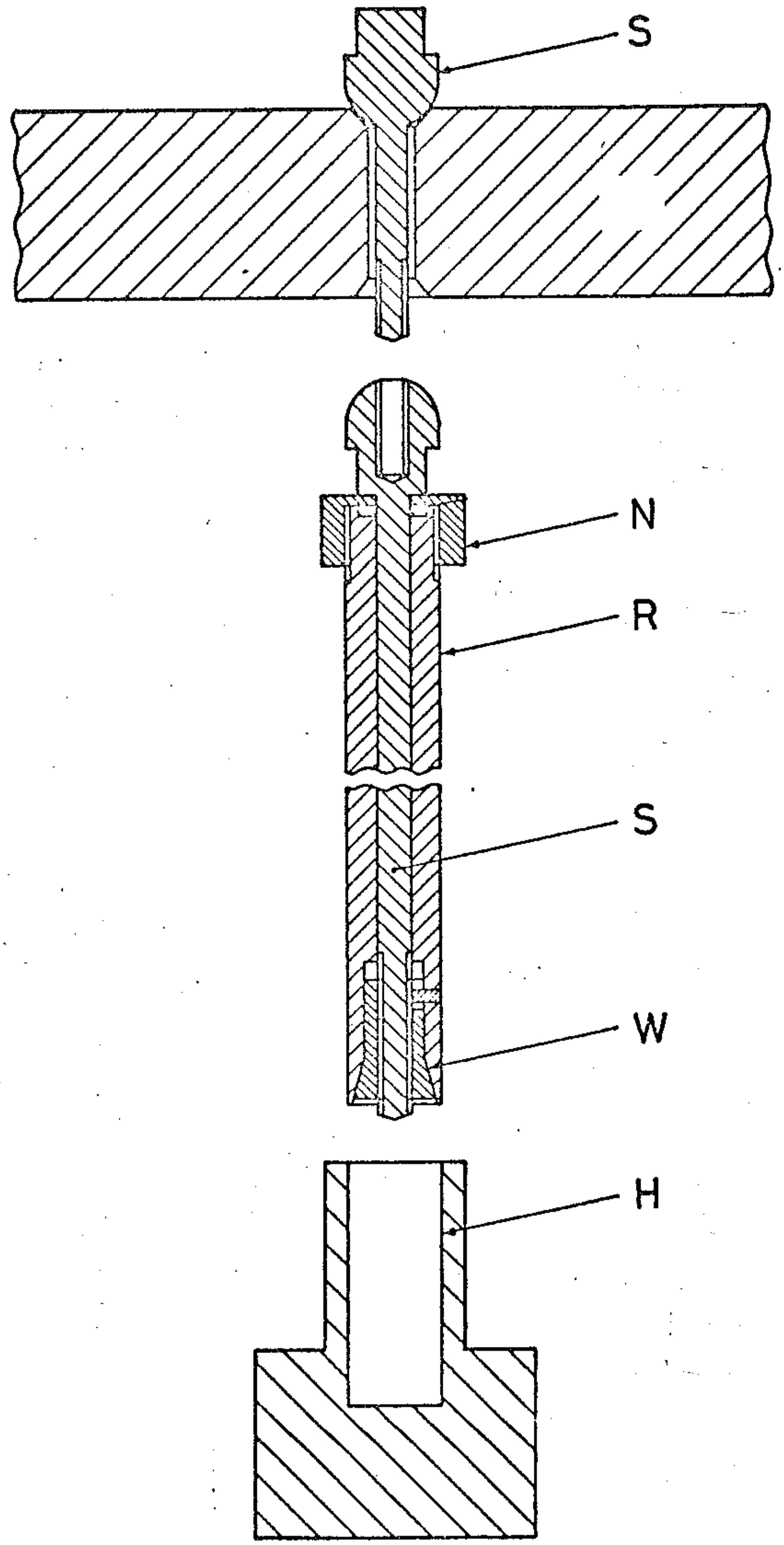

Fig. 2.6. Modified ram used in extension tests.

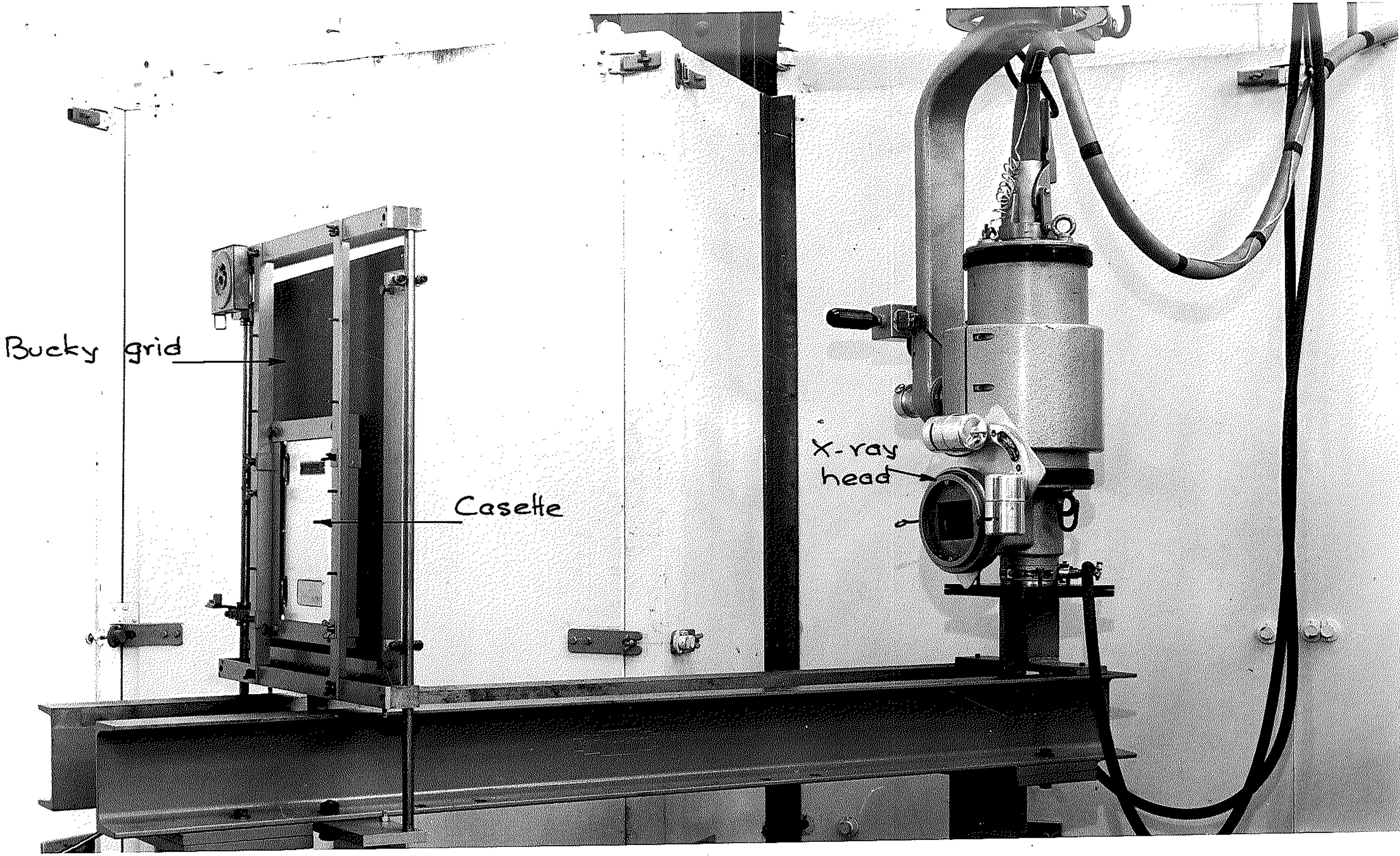

FIG.2.8 MECHANISM TO MOVE BUCKY GRID

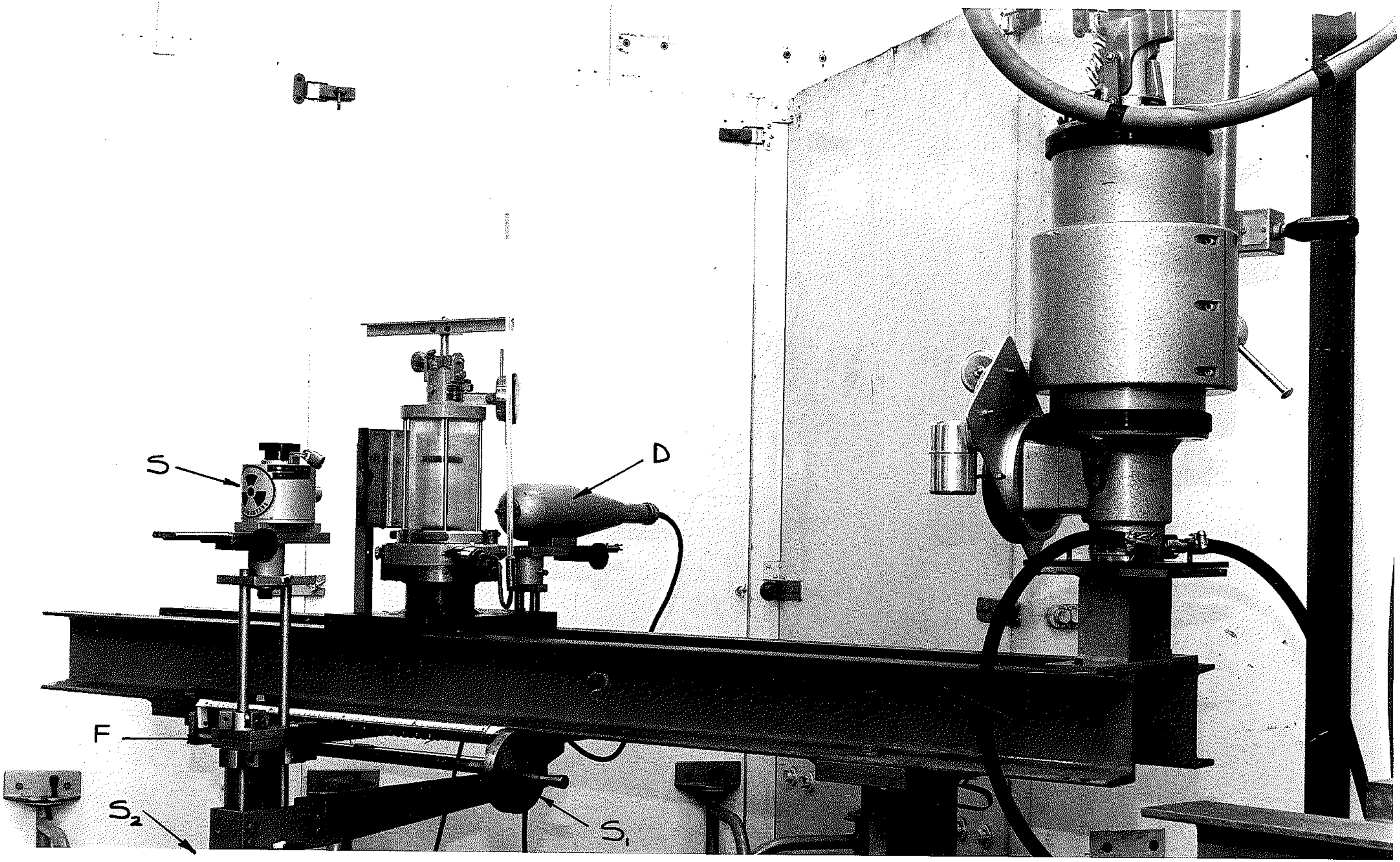

FIG. 2.9 GAMMA RAY APPARATUS MOUNTED ON TRIAXIAL TEST BED

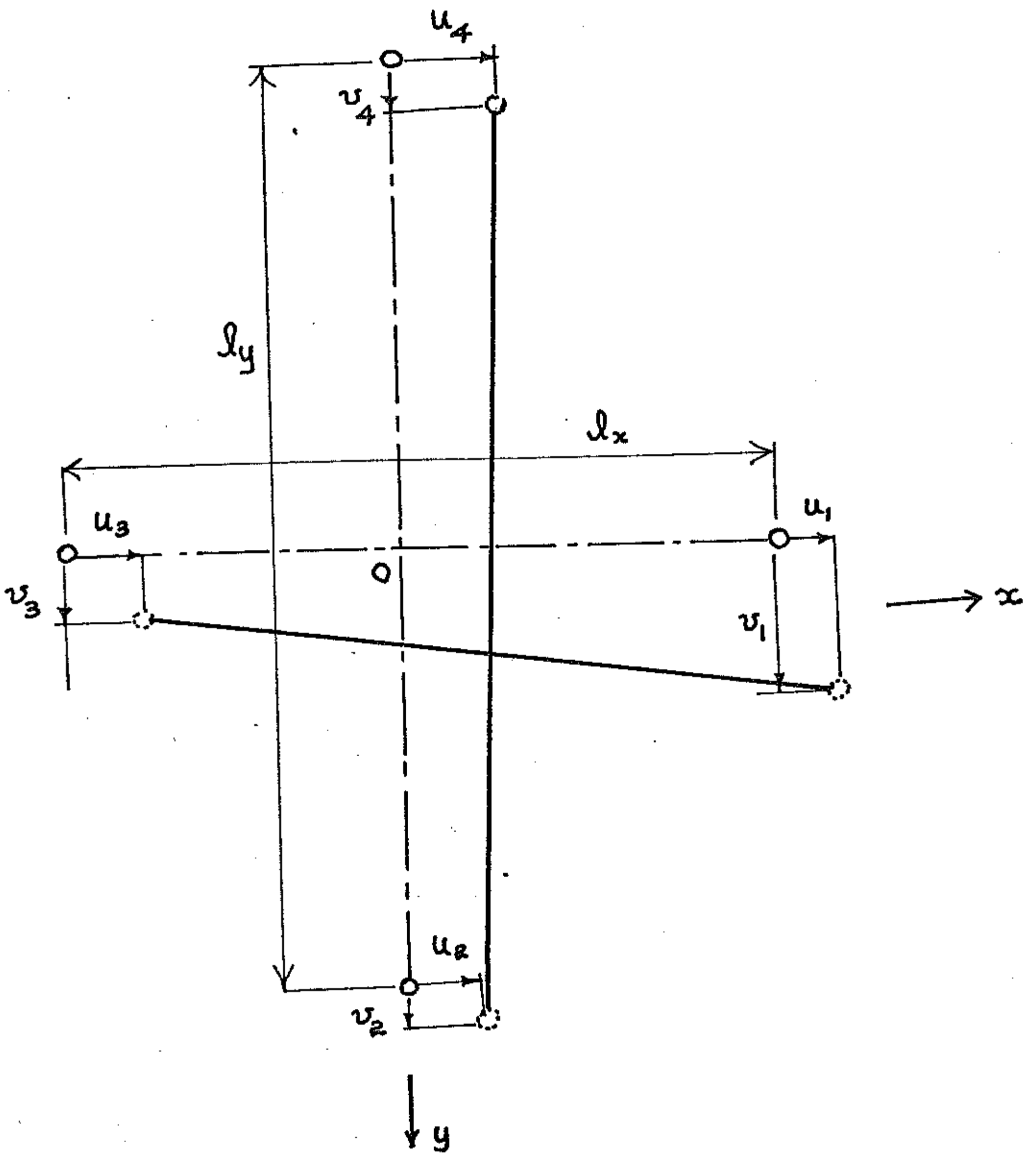

Fig. 2.IO. Incremental displacement of a mesh.
(After Roscoe Arthur James (I963))

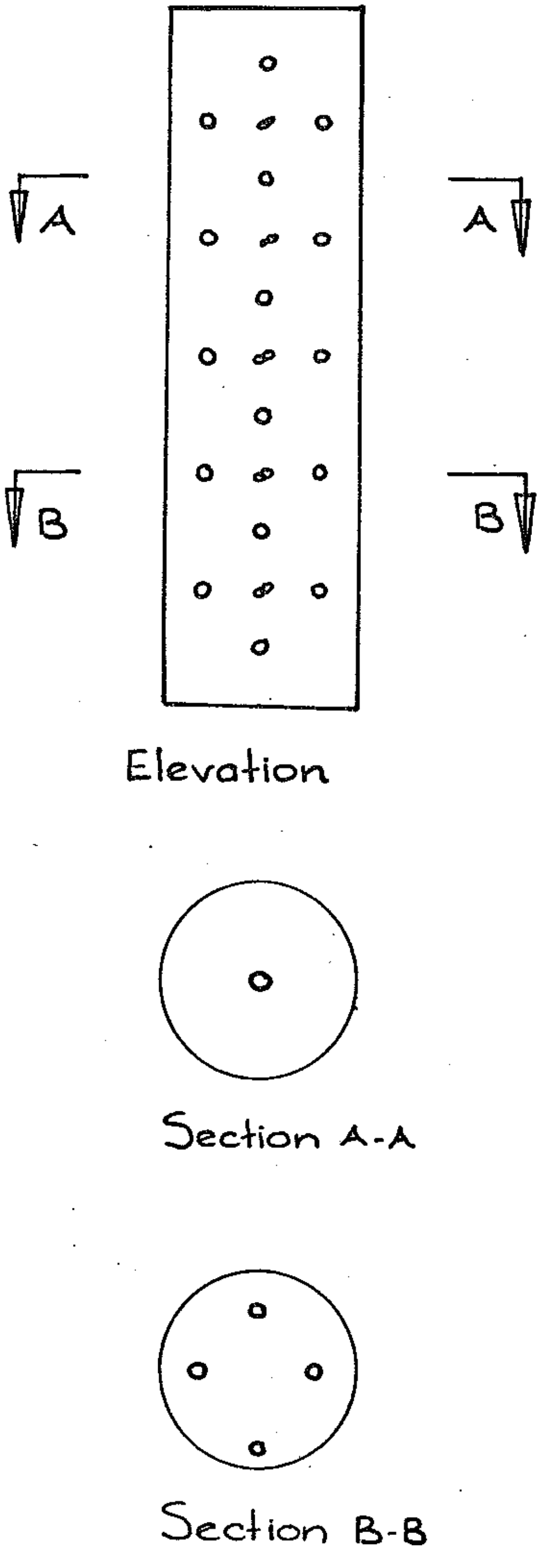

Fig. 2.11. Arrangement of lead markers used by Sirwan (1965) in triaxial sample of sand.

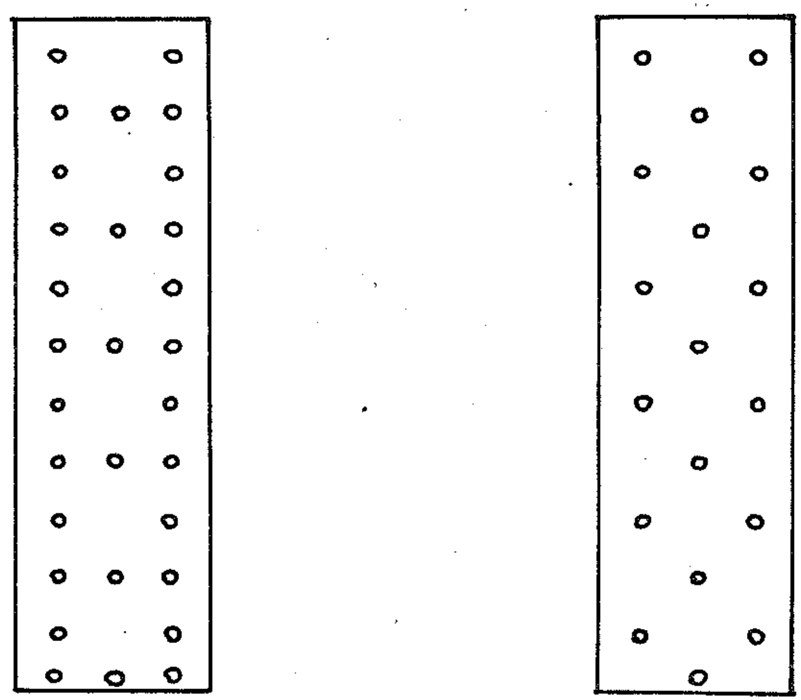

(a) Plane 1 (b) Plane 2

Fig. 2.12 (a-b) Arrangement of lead markers in two mutually perpendicular planes 1 and 2.

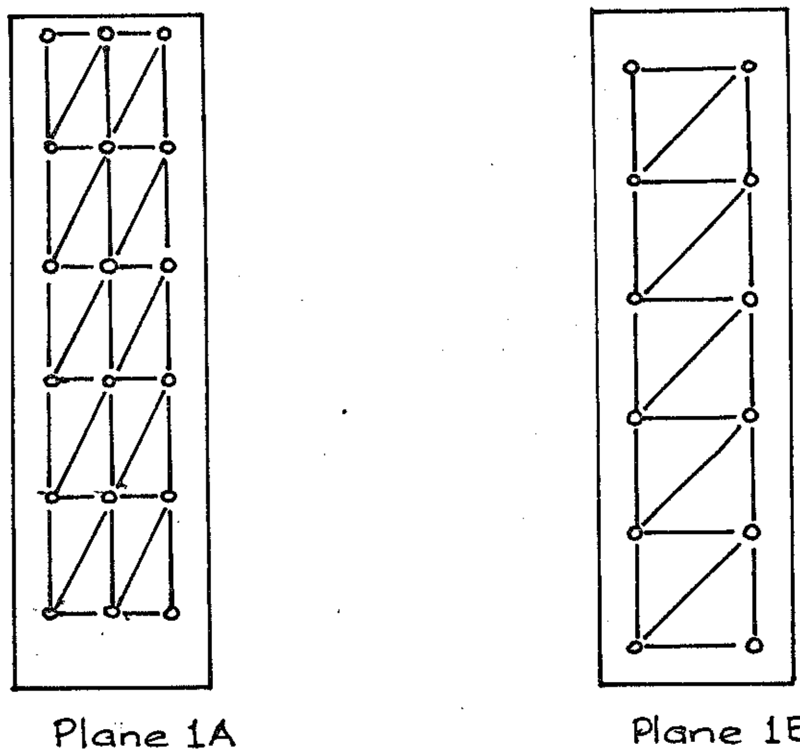

Fig. 2.13. Grouping of markers in plane 1 into two sets 1A and 1B for computation purpose.

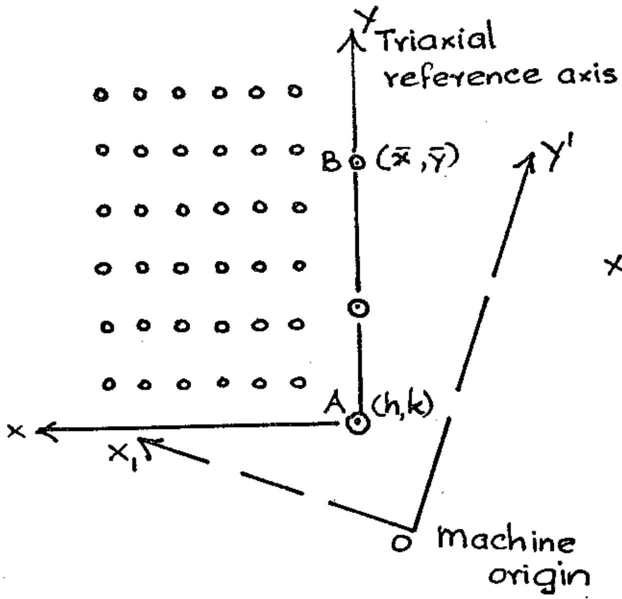

(i) Measured co-ordinates with respect to machine axis.

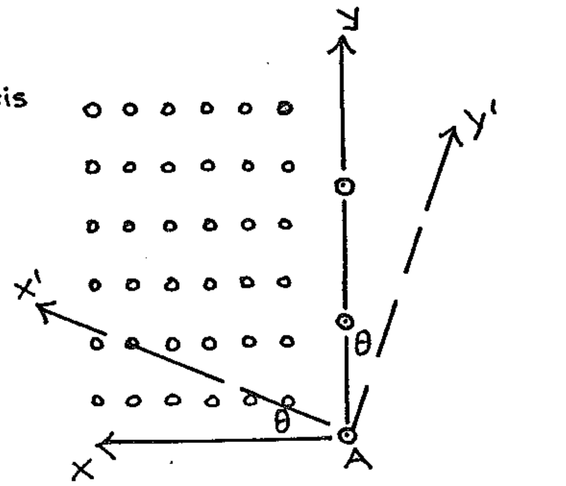

(ii) Shift of origin

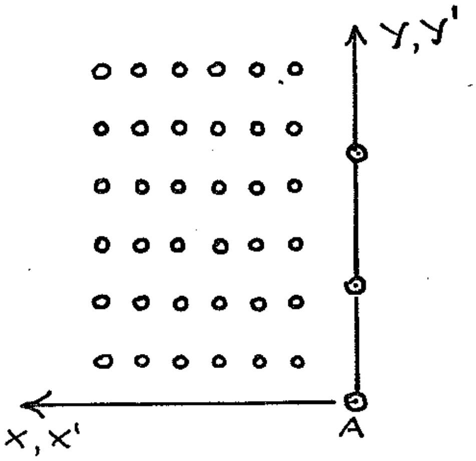

(iii) Shift and rotation of machine axes to coincide with triaxial reference axes.

Fig. 2.14. Procedure for the calculation of the co-ordinates of the lead markers.

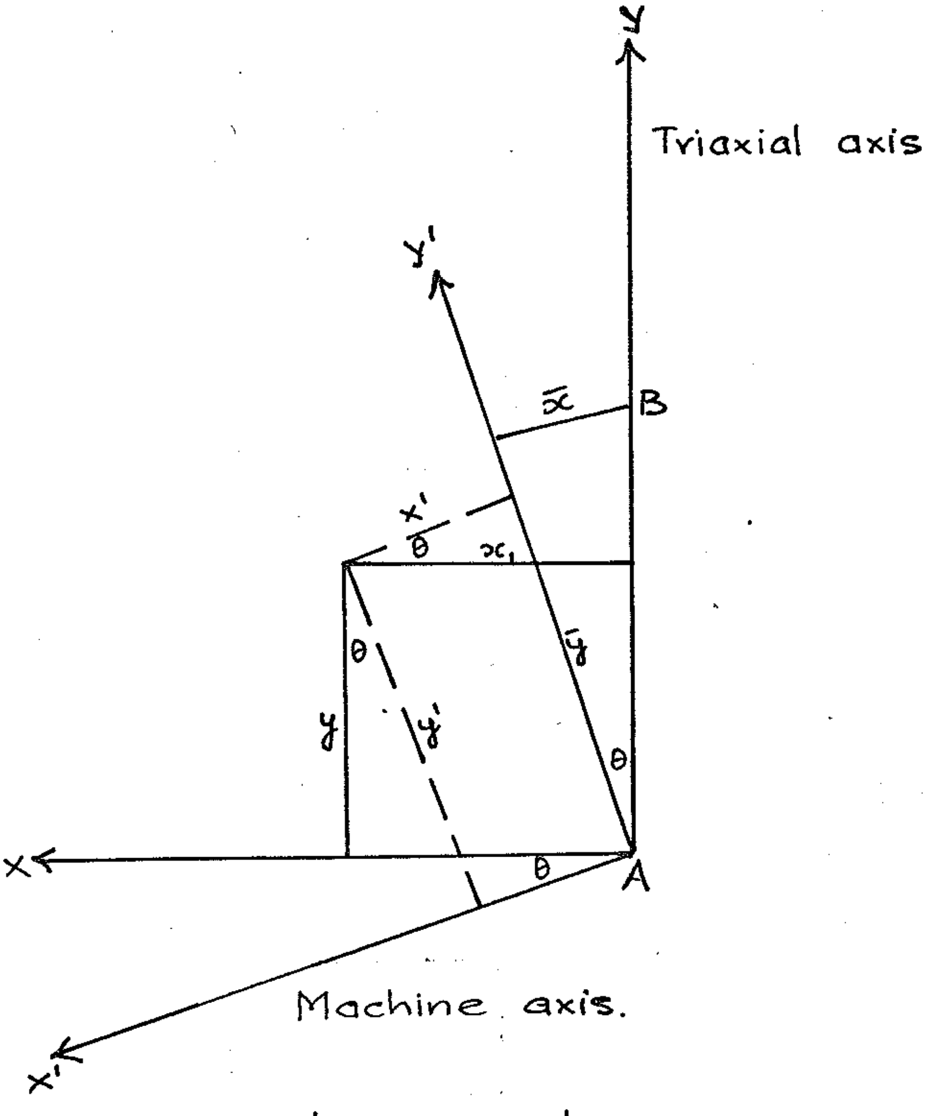

$$x = x' \cos\theta + y' \sin\theta$$
$$y = y' \cos\theta - x' \sin\theta.$$
and $$\tan\theta = \frac{\bar{x}}{\bar{y}}$$

Fig. 2.15. Transformation of co-ordinates from the machine axes to the triaxial reference axes.

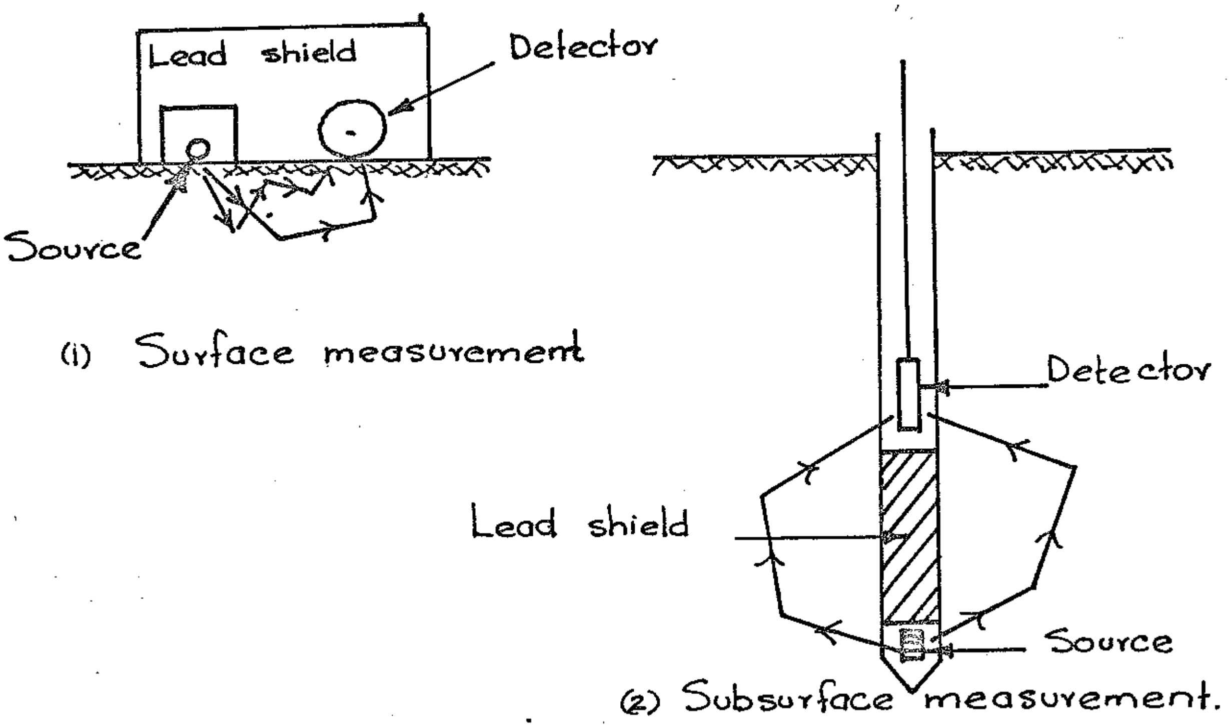

(a) Back scattering techniques

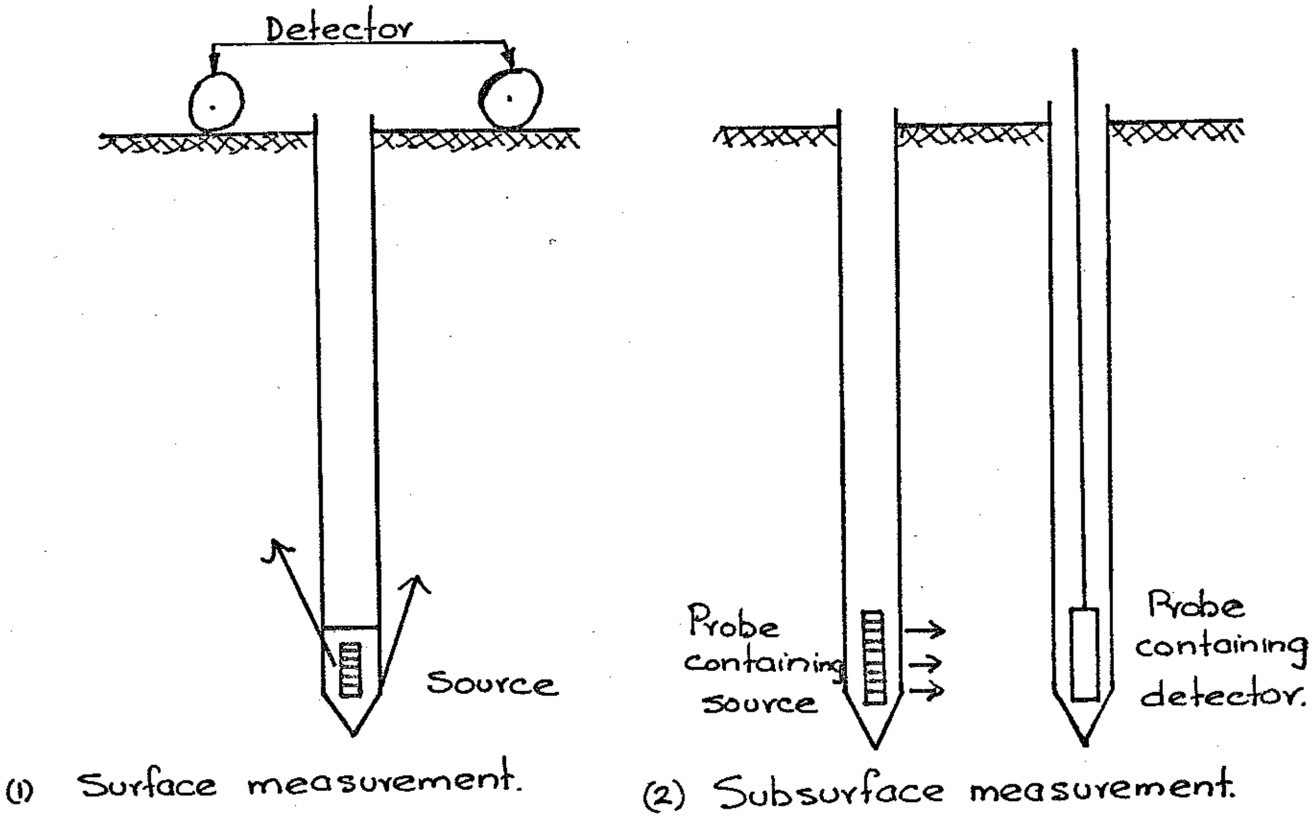

(b) Direct absorption techniques.

Fig. 3.1 (a-b) Back scattering & Direct absorption techniques for density measurements.

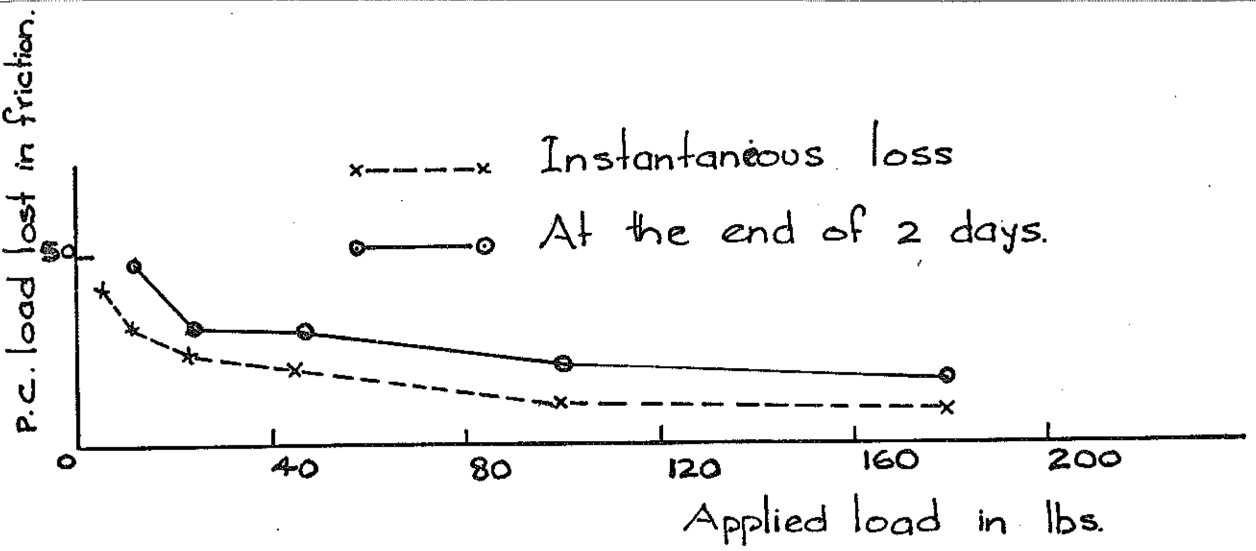

(a) Perspex Consolidometer.

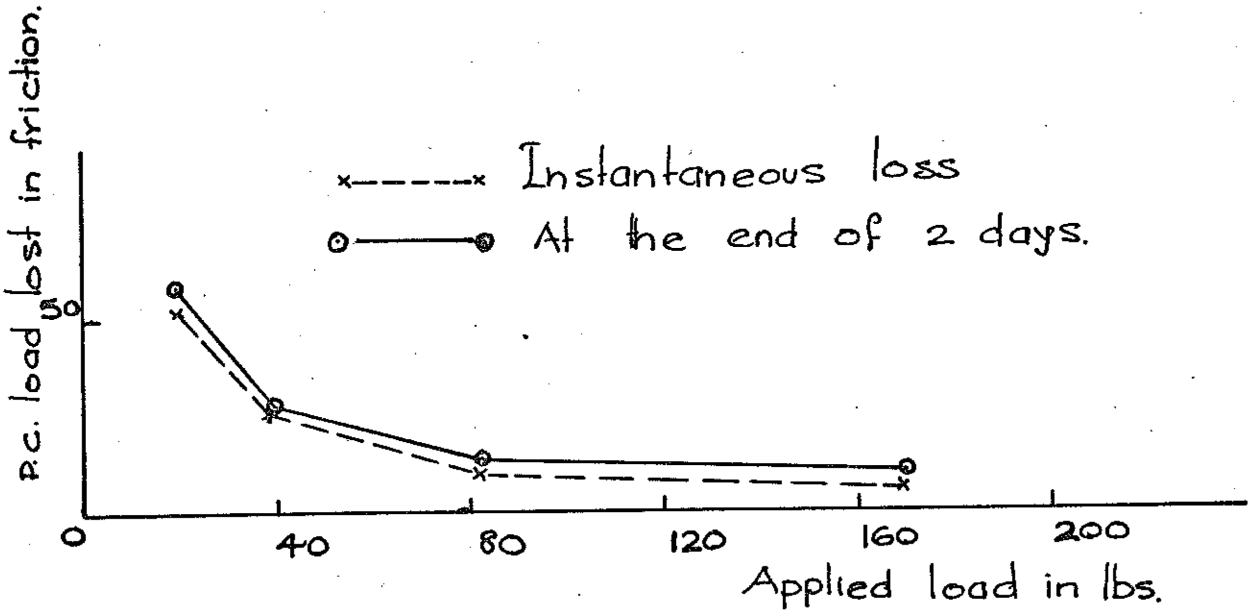

(b) Duralumin Consolidometer.

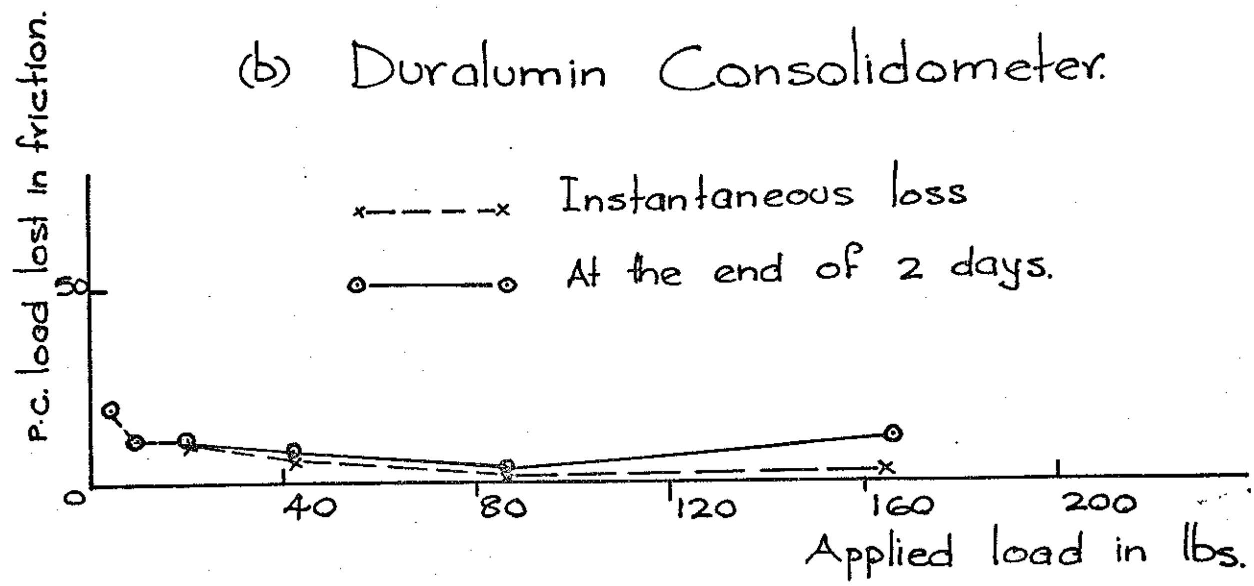

(c) Triaxial former with rubber lining

Fig. 3.2(a-c) FRICTION LOSS IN CONSOLIDOMETER

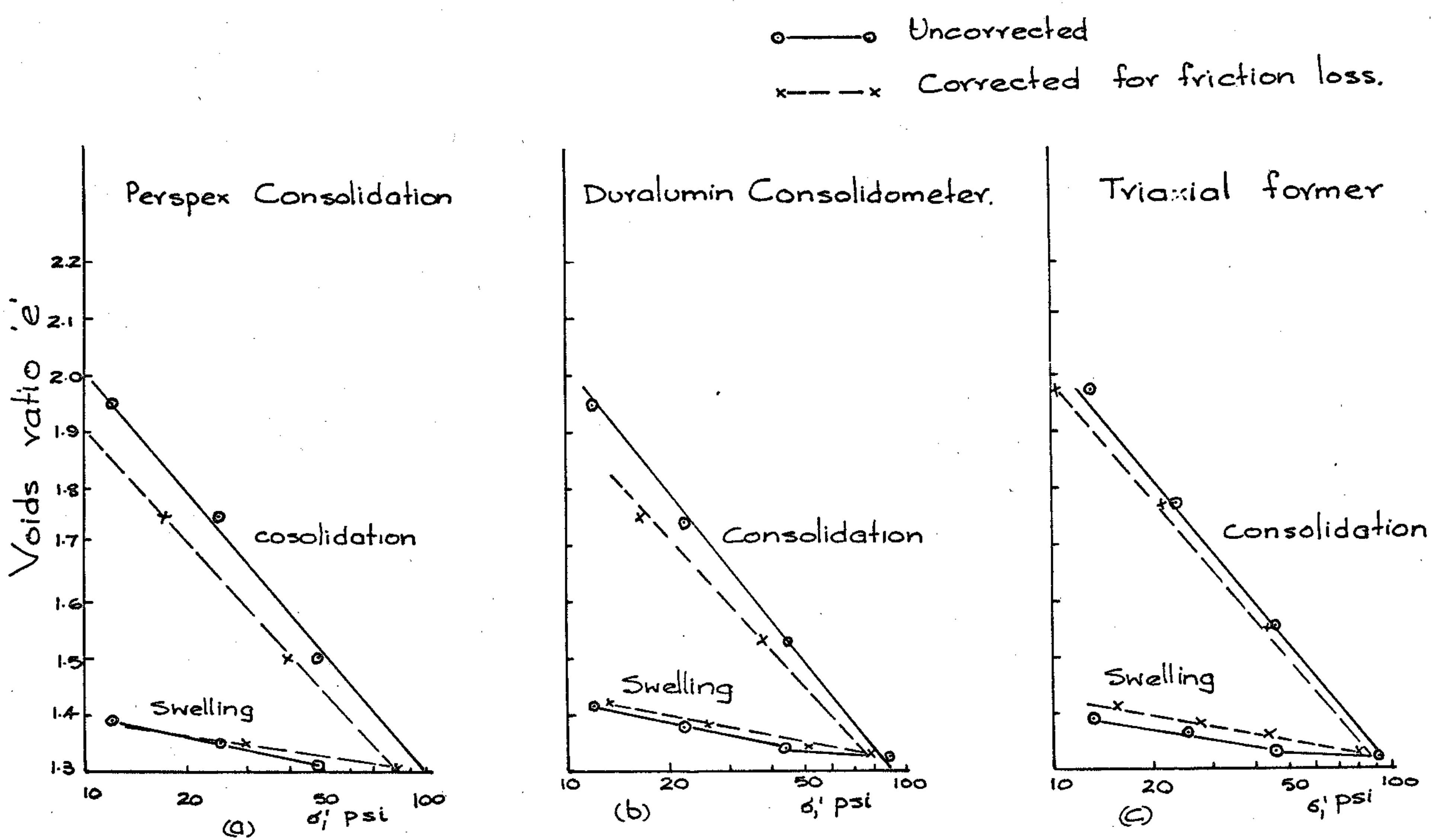

Fig. 3.3. Voids ratio Vs. Log σ_1' plot for 1-D Consolidation & swelling.

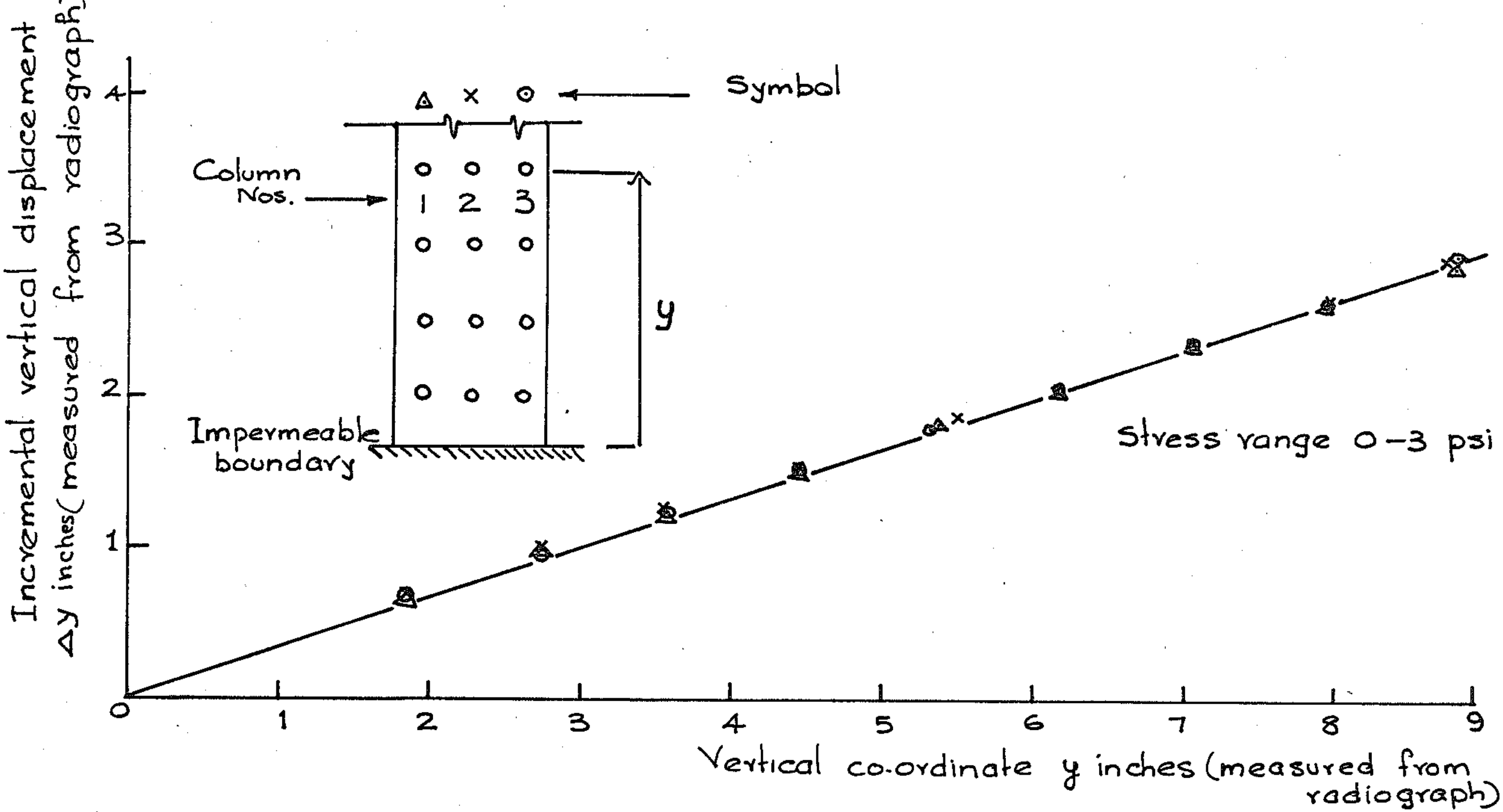

Fig. 3.4. Incremental vertical displacement of markers for first increment of stress during 1-D consolidation from slurry.

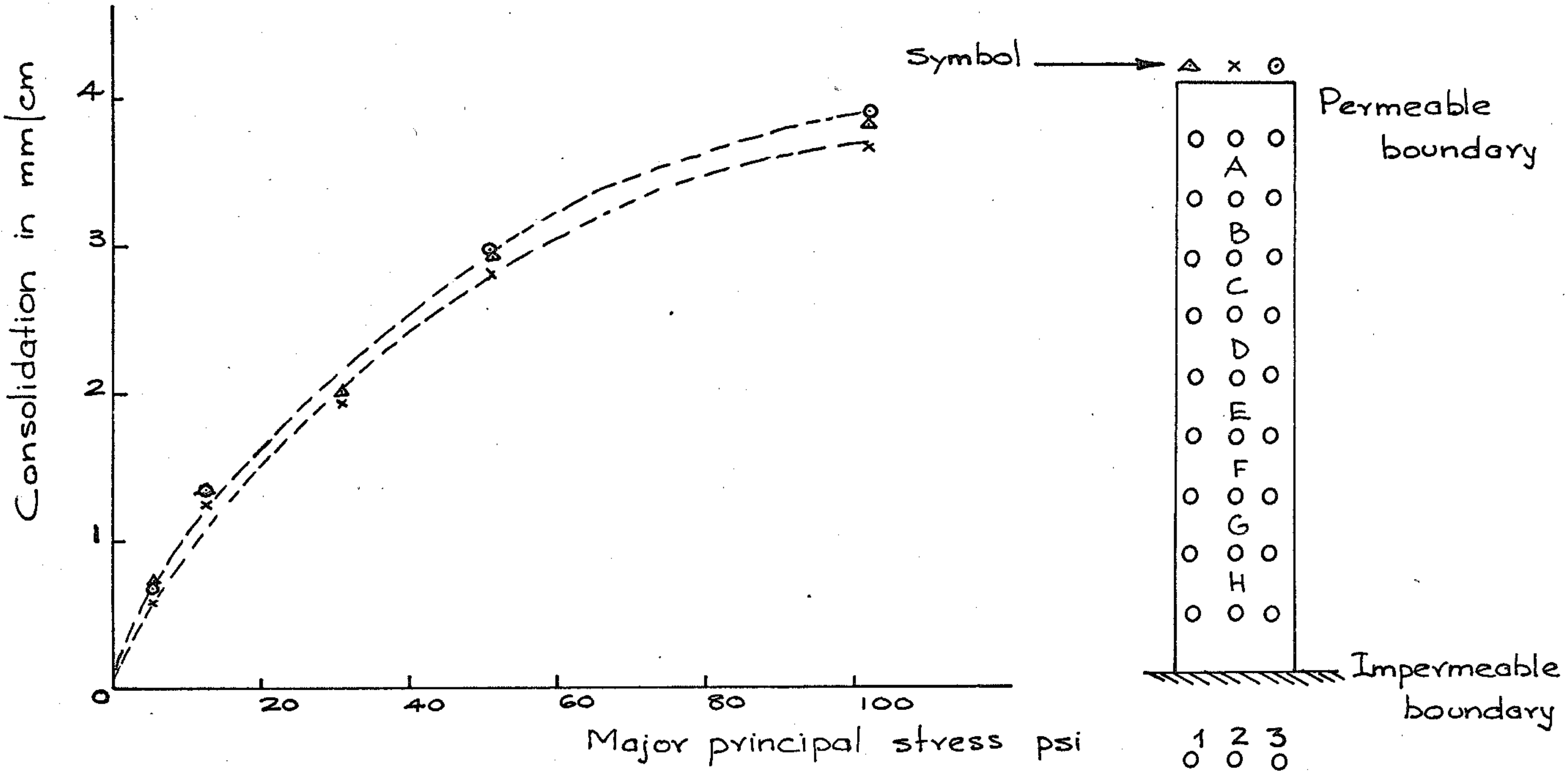

Fig. 3.5. Consolidation of 3 vertical columns in element A plotted with respect to the major principal effective stress.

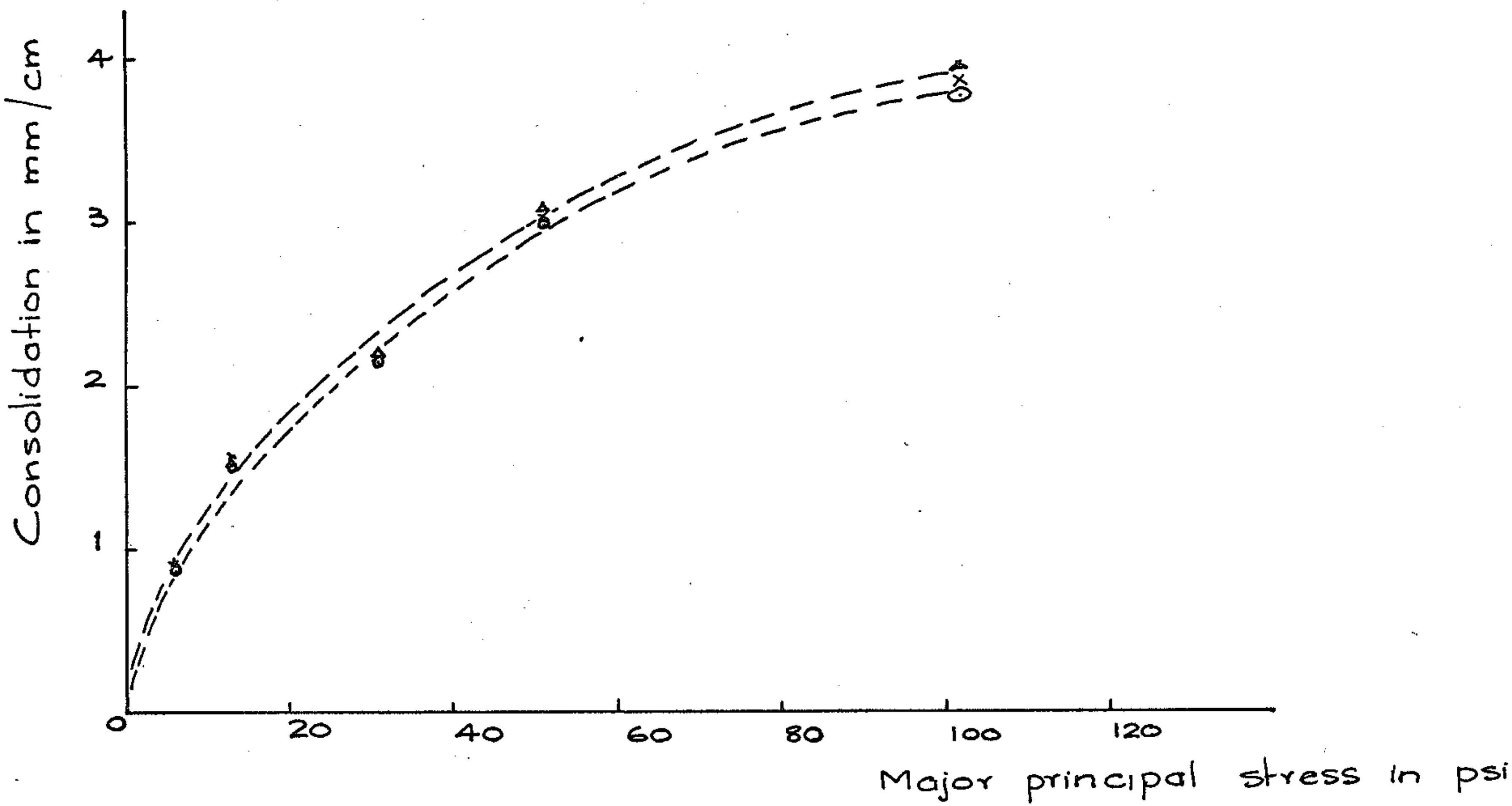

Fig. 3.6. Consolidation of 3 vertical columns in element D (See fig 35) plotted with respect to the major principal effective stress.

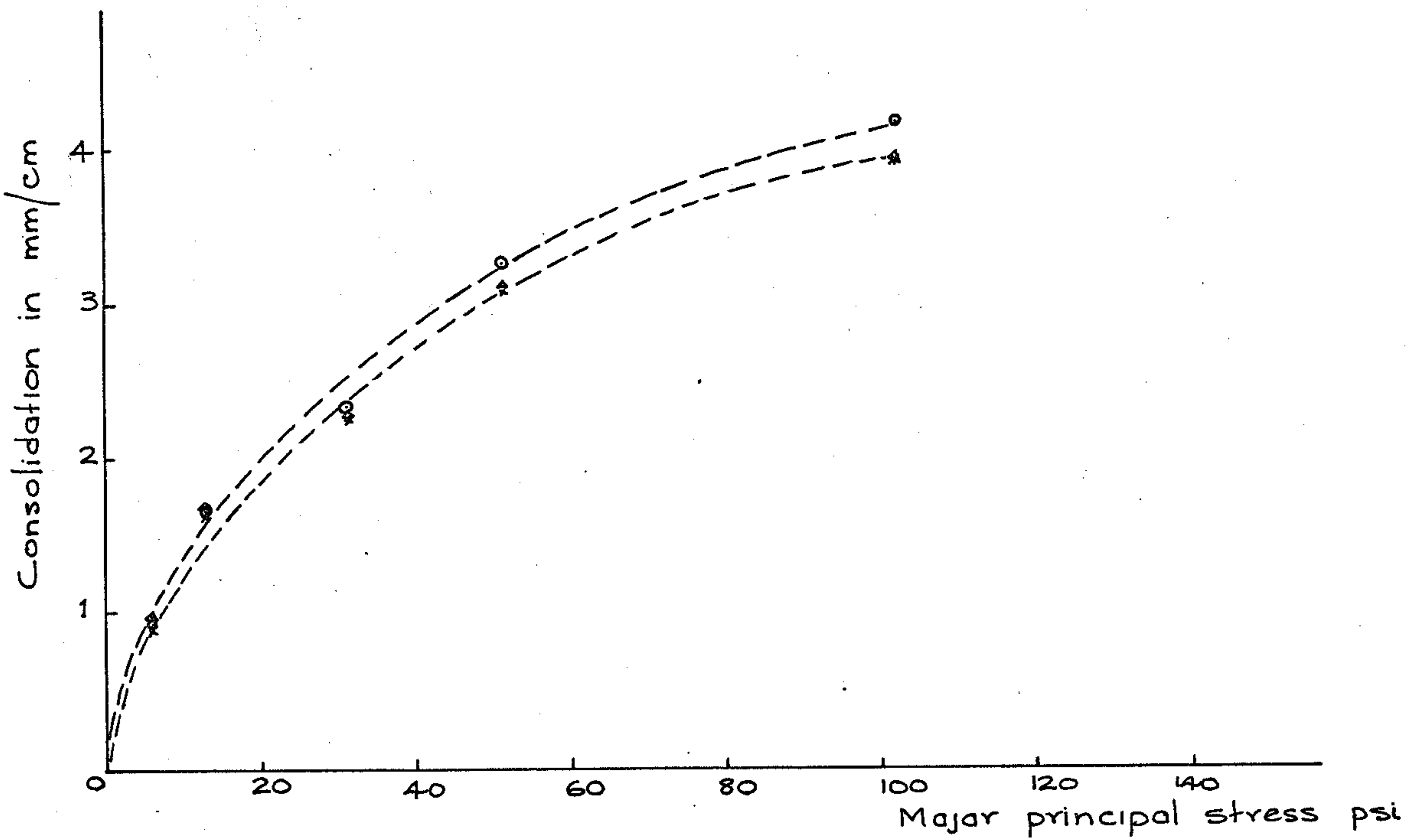

Fig. 3.7. Consolidation of 3 vertical Columns in element H (see fig. 3.5) plotted with respect to major principal effective stress.

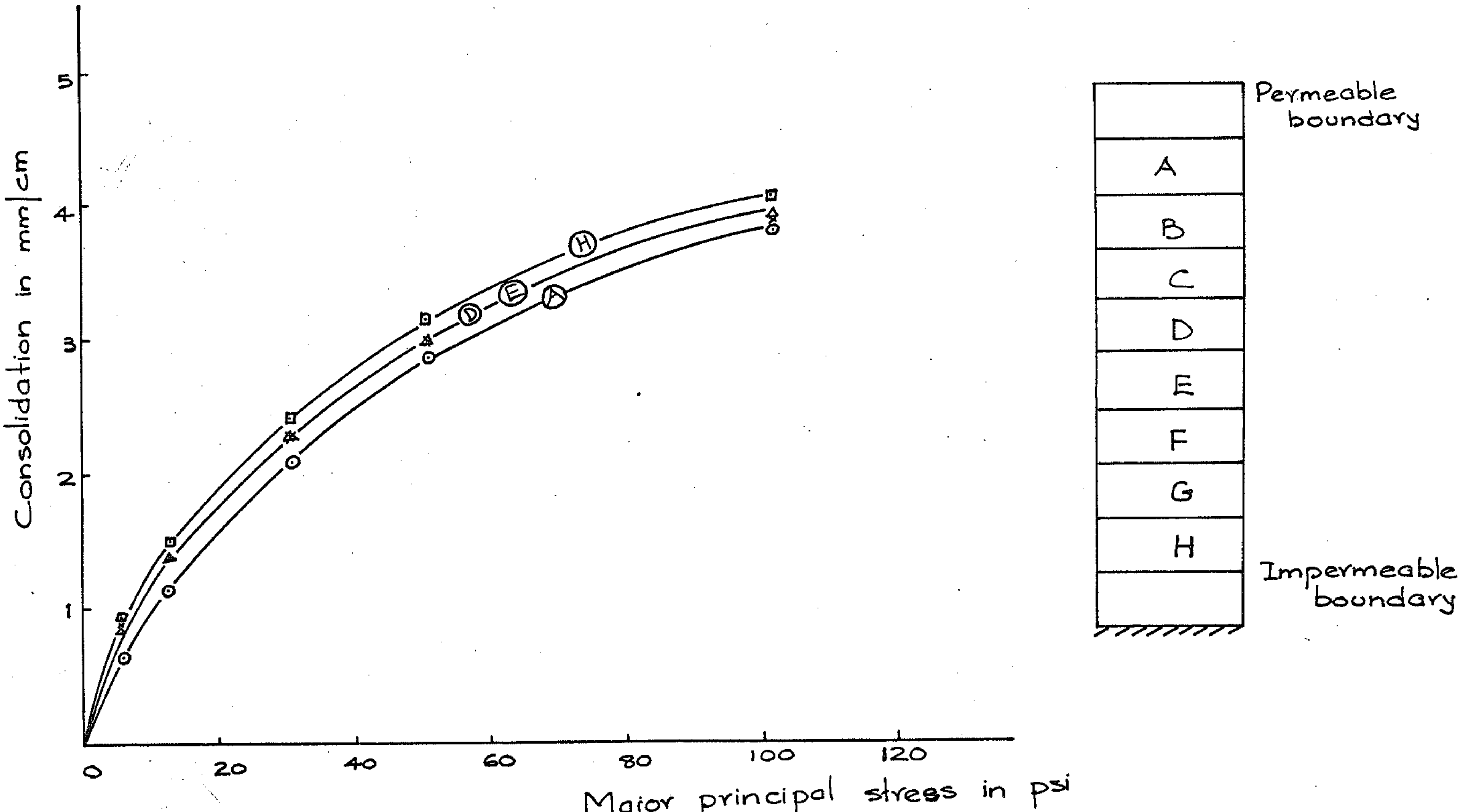

Fig. 3.8. Consolidation of 4 elements A, D, E & H plotted with respect to the major principal stress.

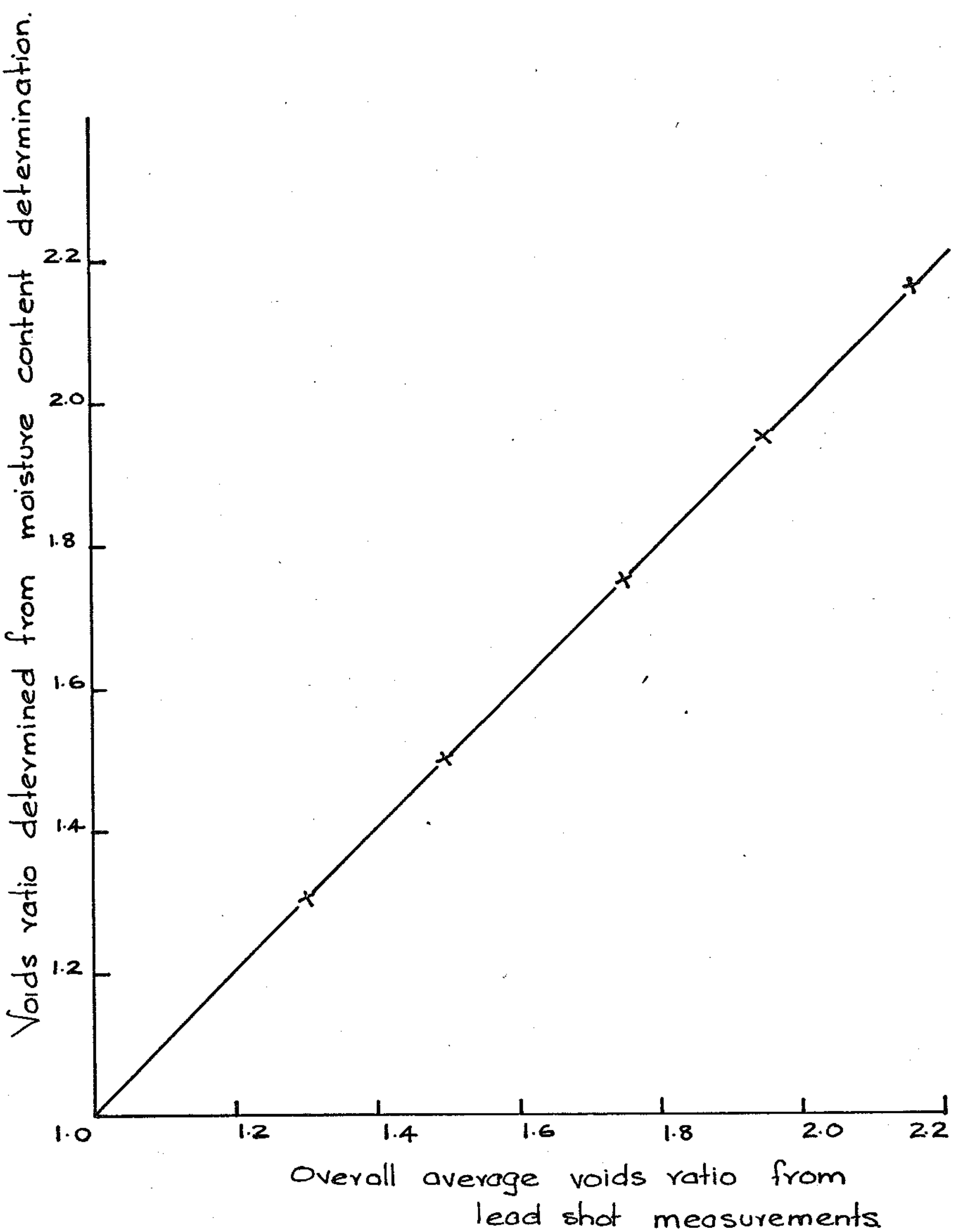

Fig. 3.9 Comparison of overall average voids-ratio computed from the local measurements and the average overall voids ratio as determined from the moisture content and the heights of the sample.

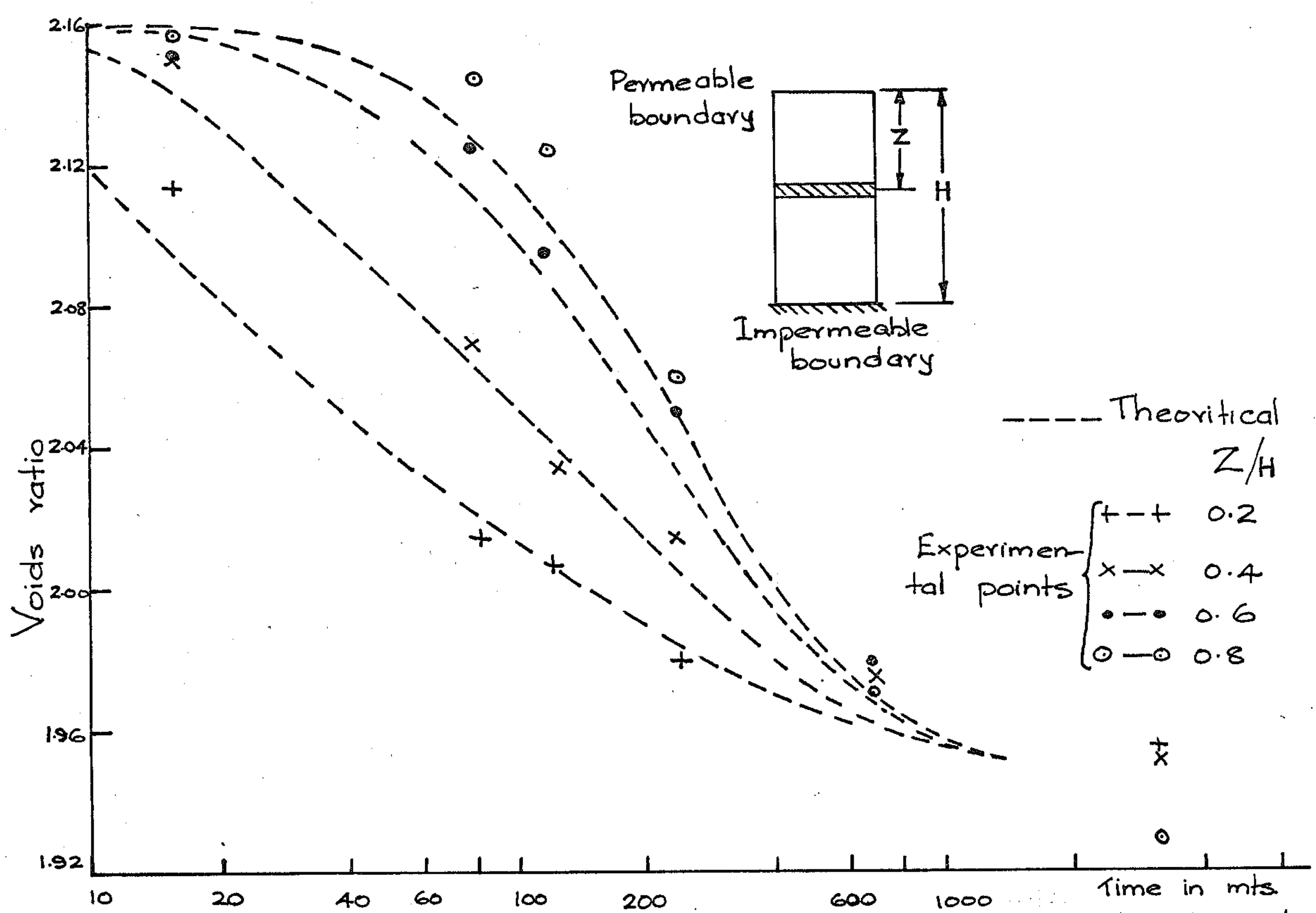

Fig. 3.10 Comparison of local voids ratios and theoretical voids ratios at different depths during pore pressure dissipation for stress increment 6 to 12 p.s.i

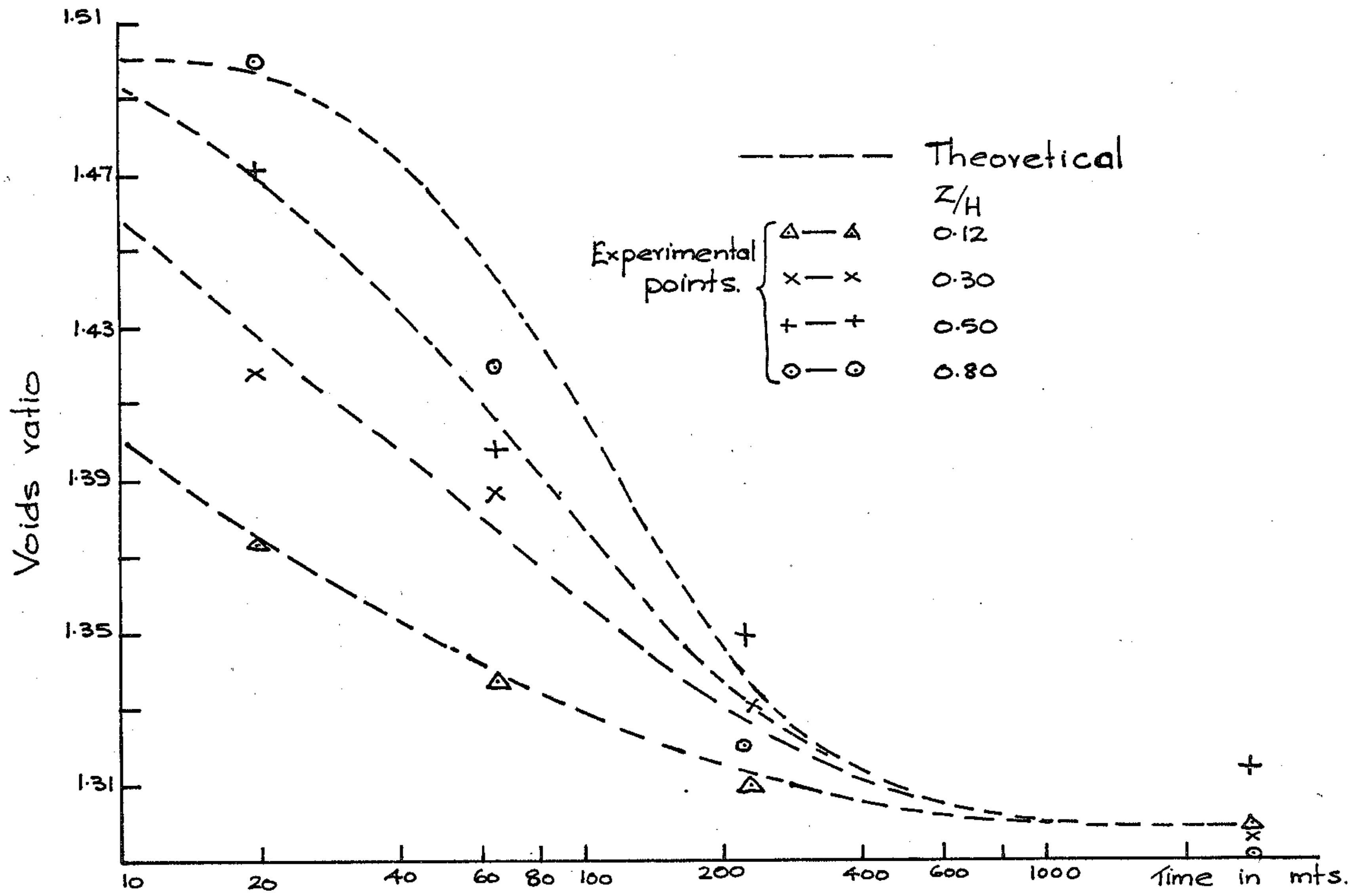

Fig. 3.11. Comparison of local voids ratios and theoretical voids ratios at different depths during pore pressure dissipation for stress increment 51 to 102 psi.

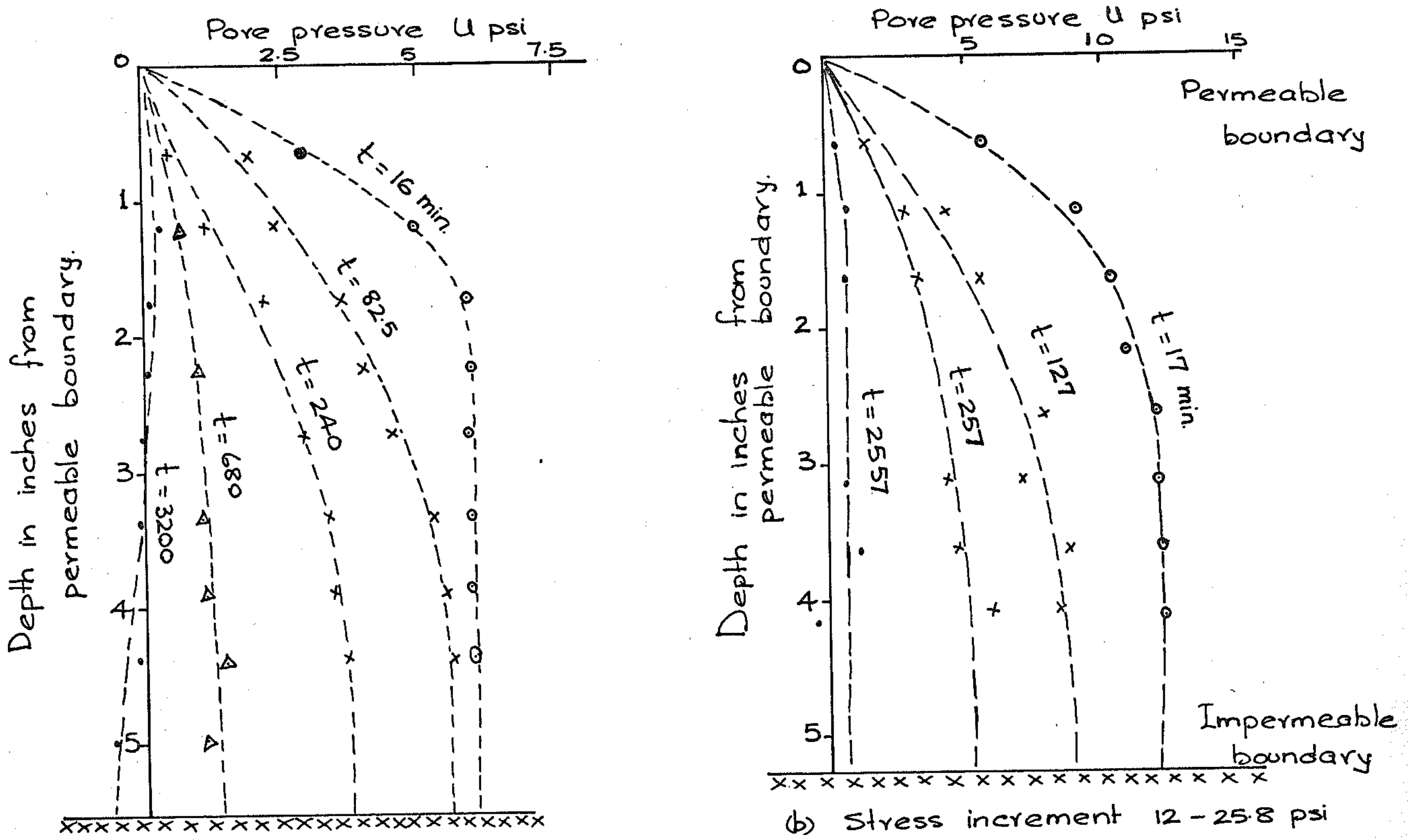

(a) Stress Increment 6 – 11.9 psi

(b) Stress increment 12 – 25.8 psi

Fig. 3.12. Pore pressure isochrones determined from local measurements of strains for 2 stress increments.

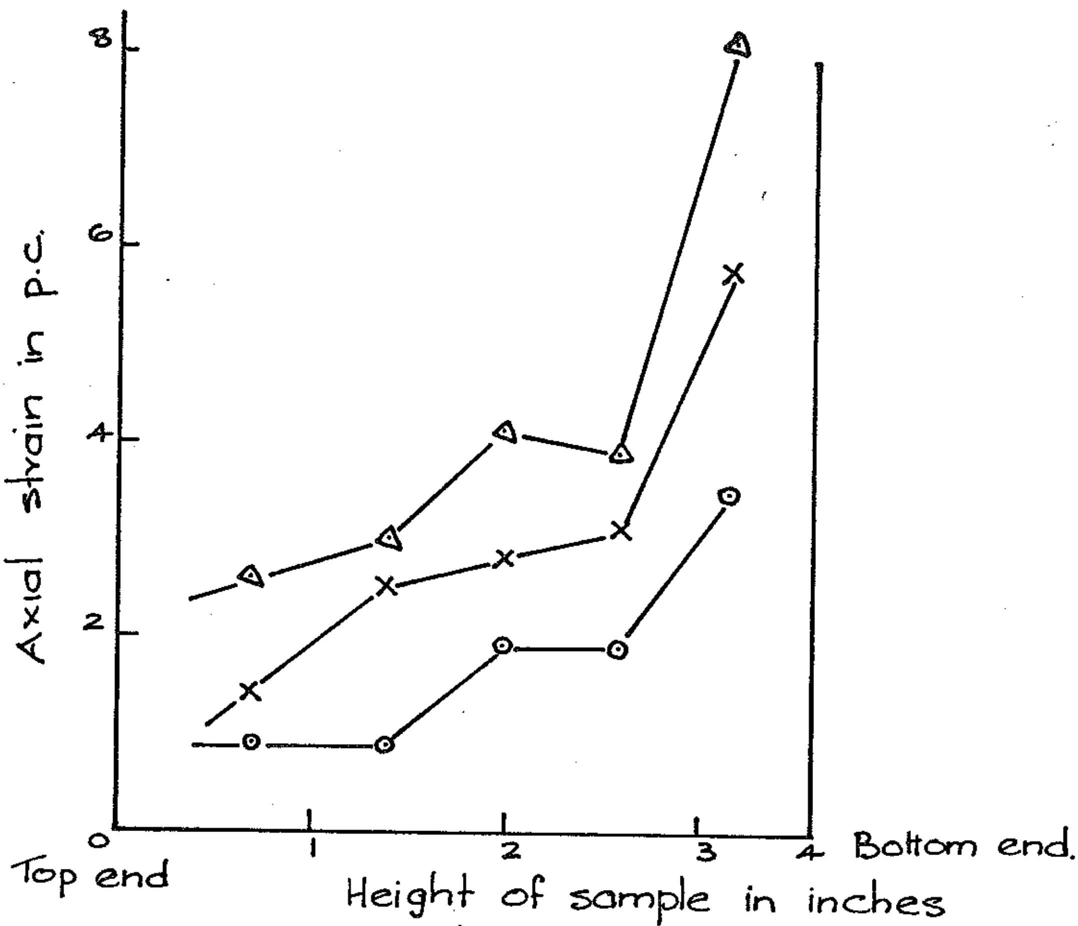

3.13 (a) Axial strain distribution

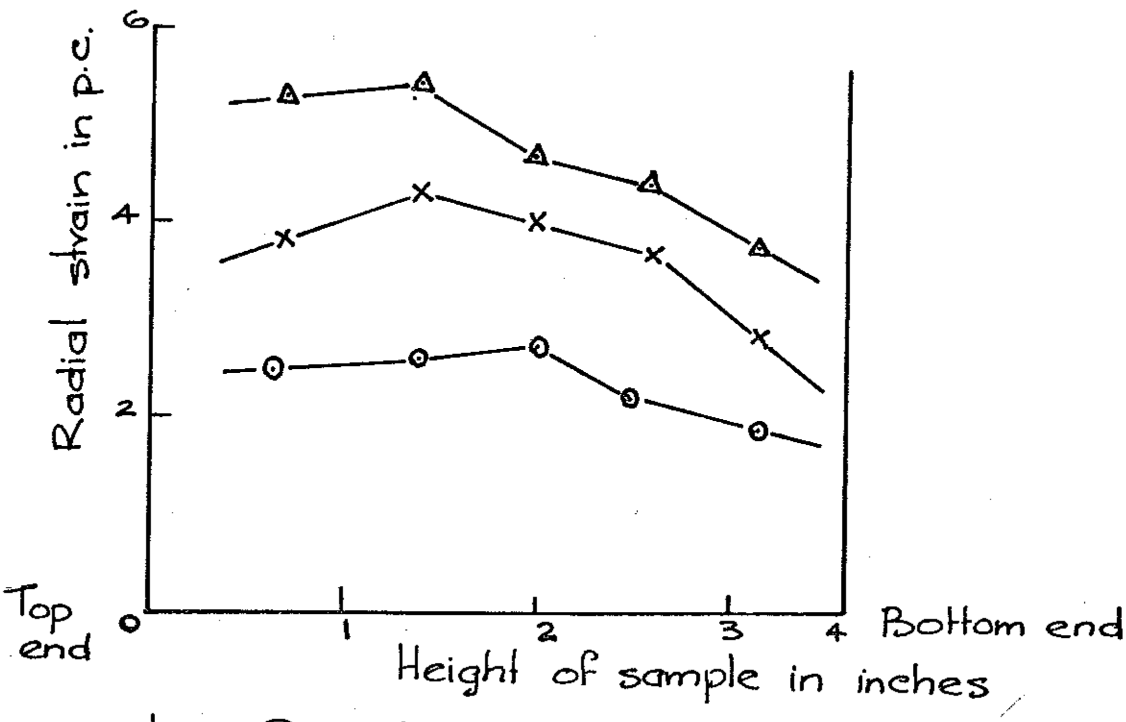

3.13 (b) Radial strain distribution

See overleaf

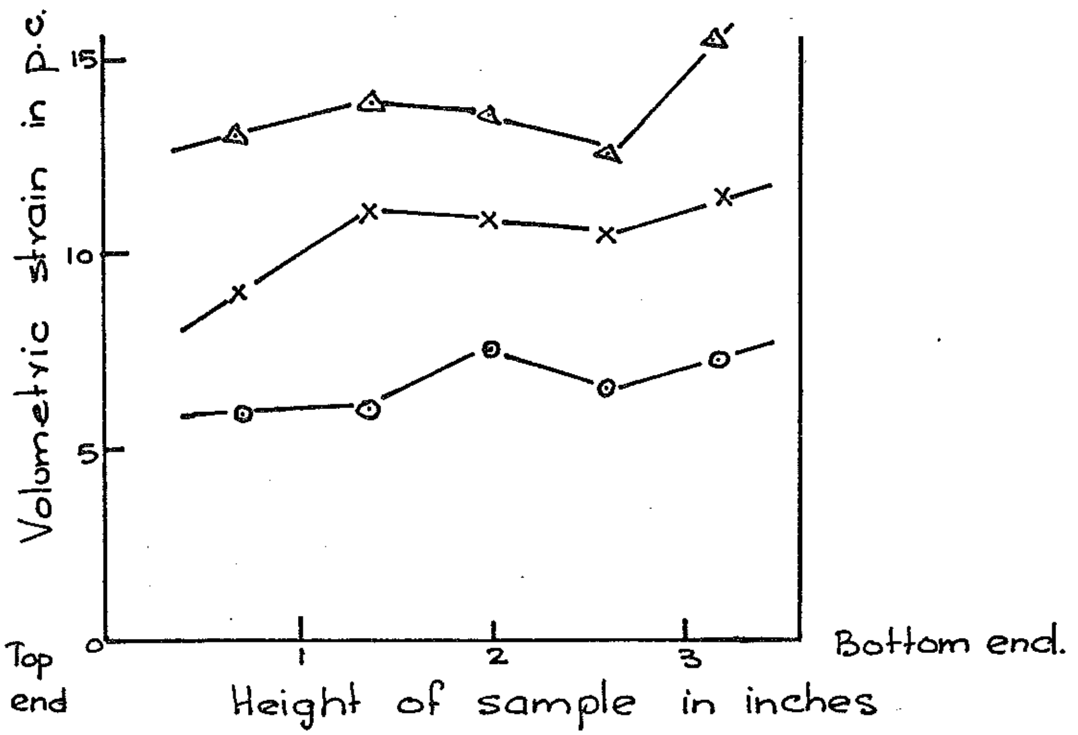

3.13 (c) Volumetric strain distribution

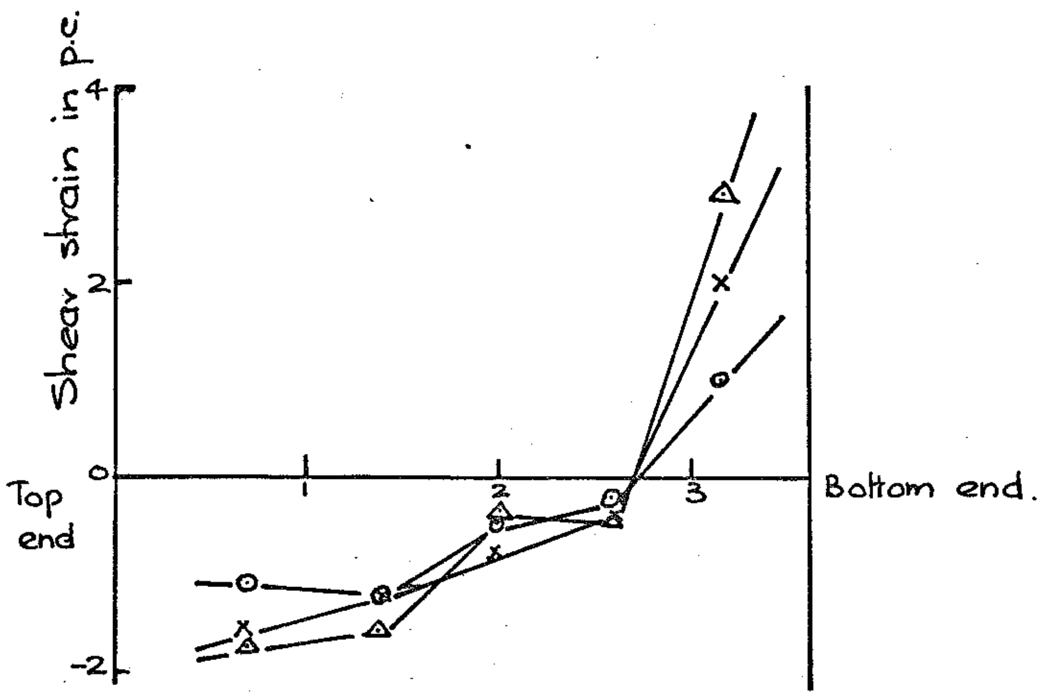

3.13 (d) Shear strain distribution.

Fig. 3.13 (a-d) Strain distributions plotted against height of sample during isotropic consolidation in a 1.5 inch diameter specimen contained between conventional frictional ends.

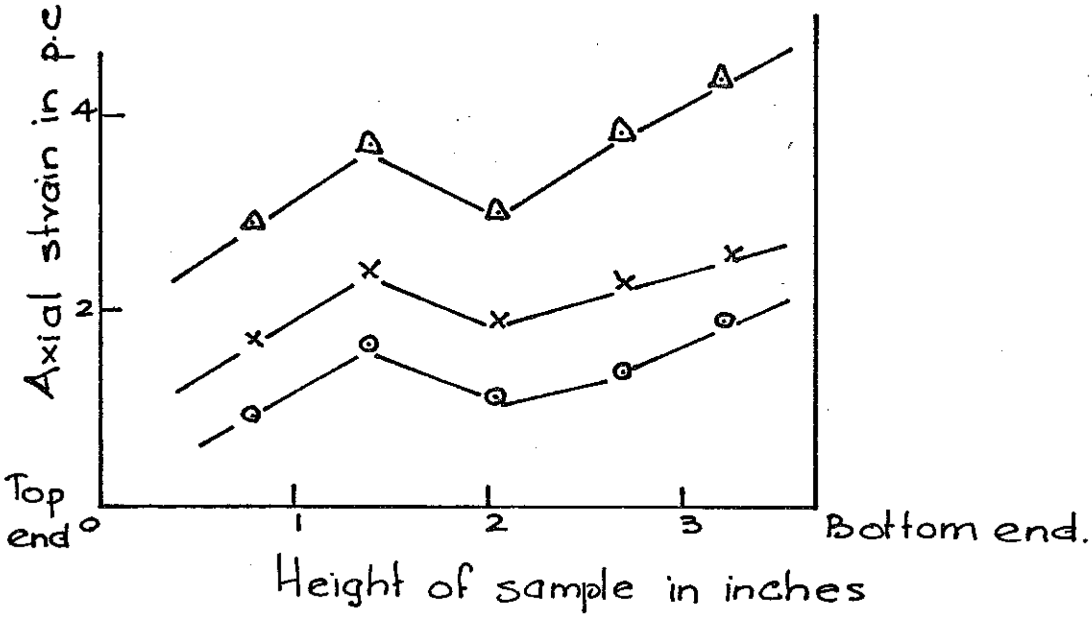

Fig. 3.14 (a) Axial strain distribution

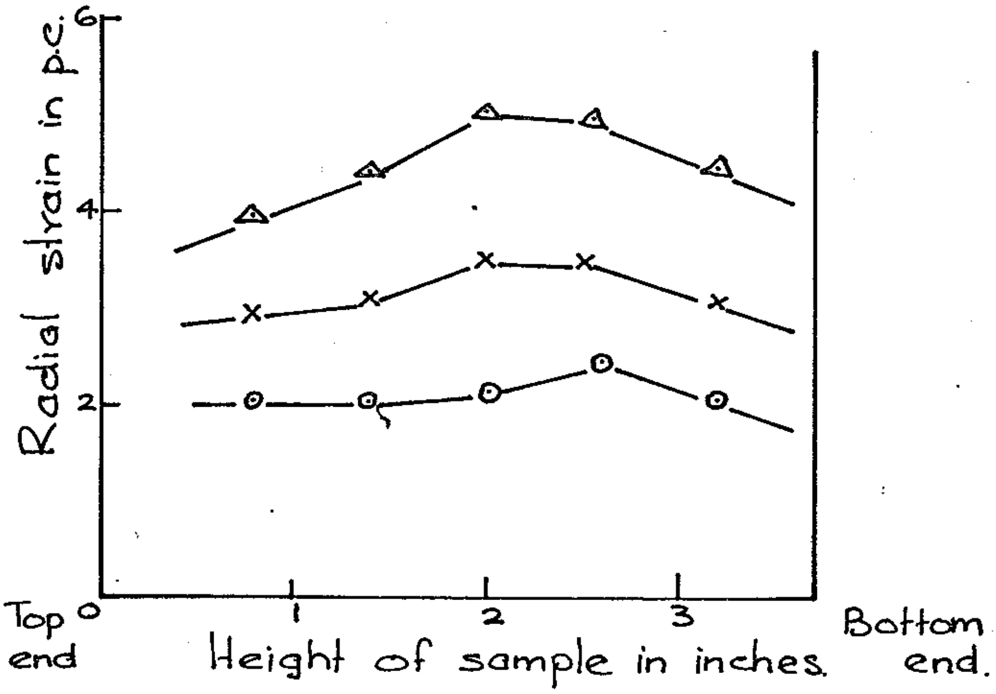

Fig. 3.14 (b) Radial strain distribution

See overleaf

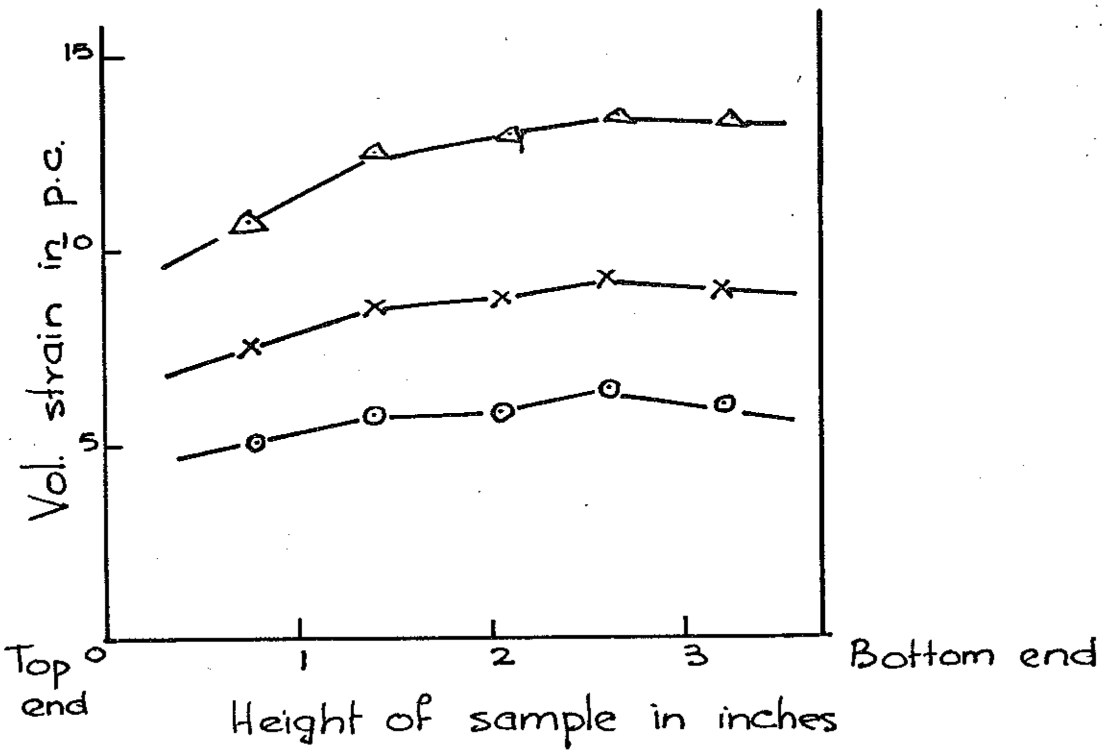

3.14 (c) Volumetric strain distribution.

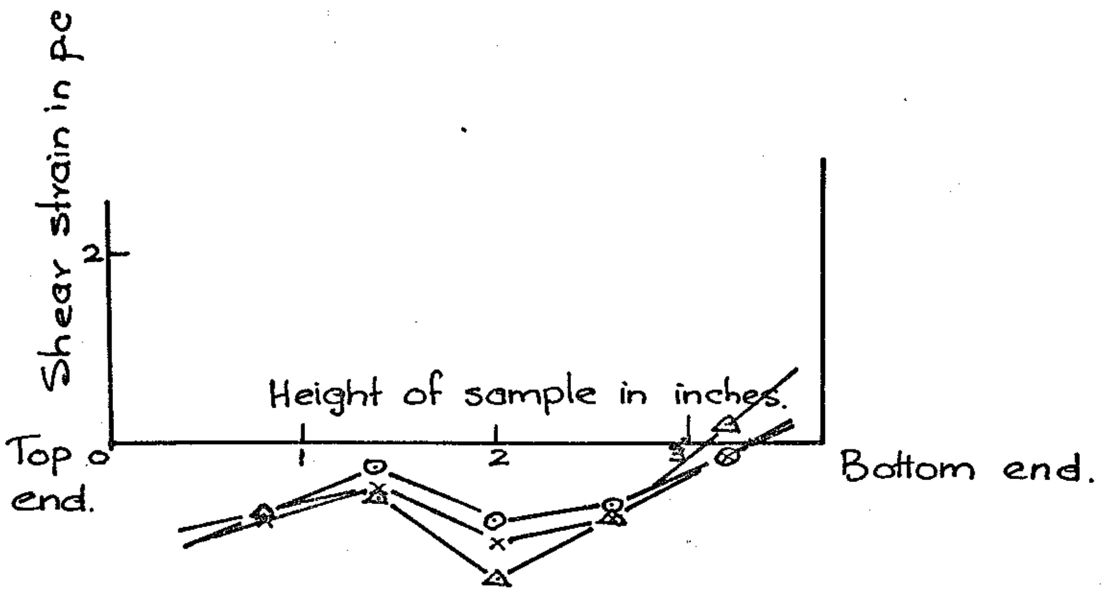

3.14 (d) Shear strain distribution

Fig. 3.14 (a-d): Strain distributions plotted against height of sample during isotropic consolidation in a 1.5 inch diameter specimen contained between conventional lubricated ends.

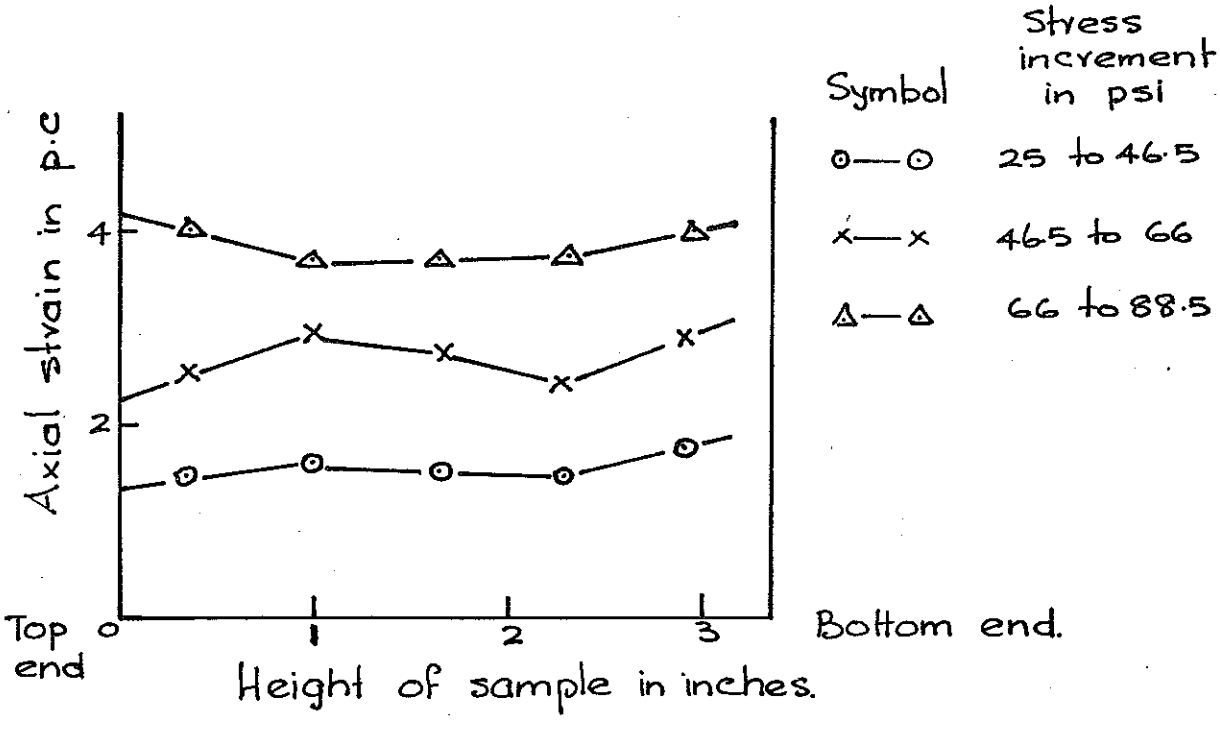

3.15 (a) Axial strain distribution

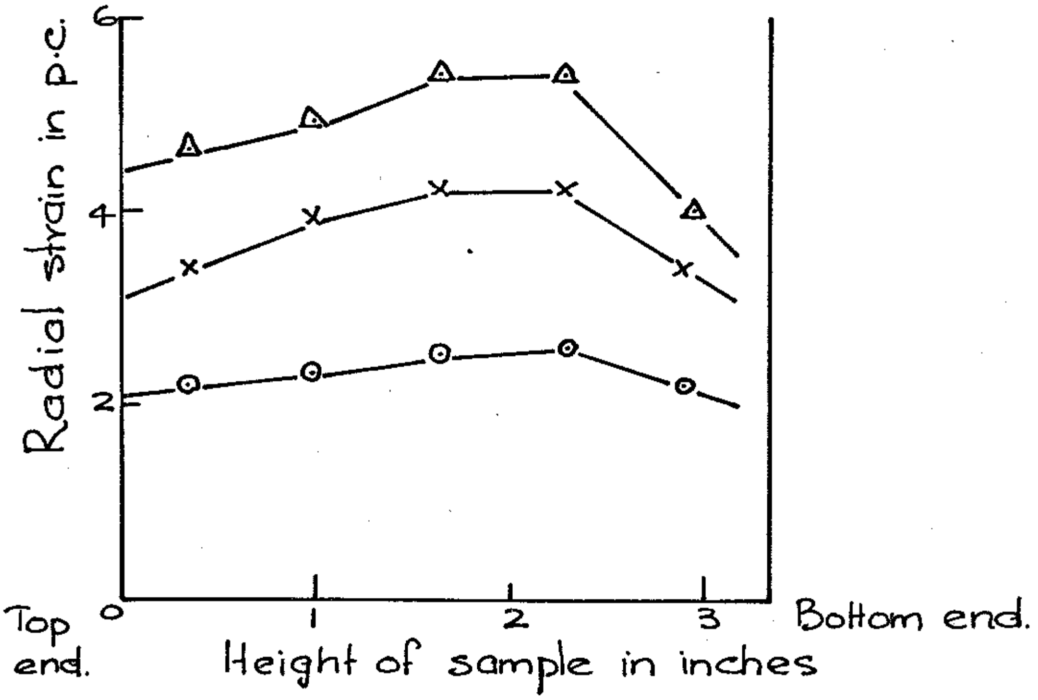

3.15 (b) Radial strain distribution

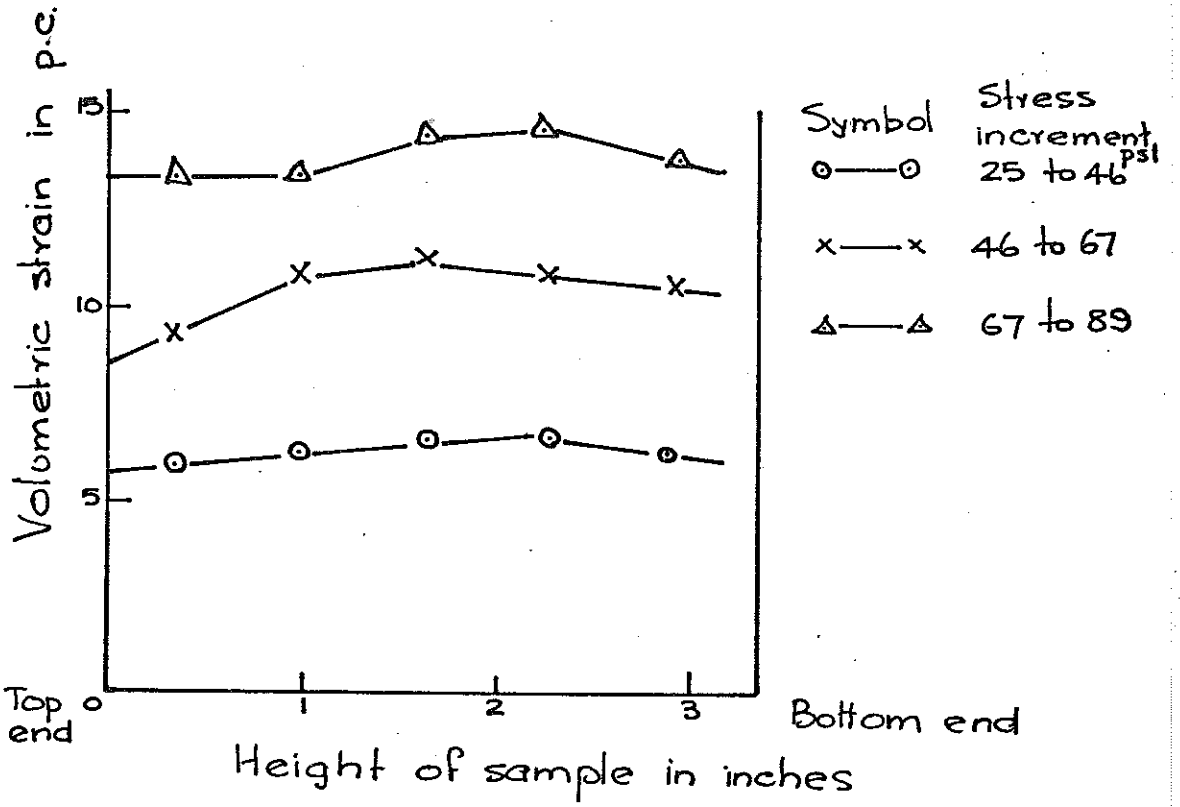

3.15 (c) Volumetric strain distribution

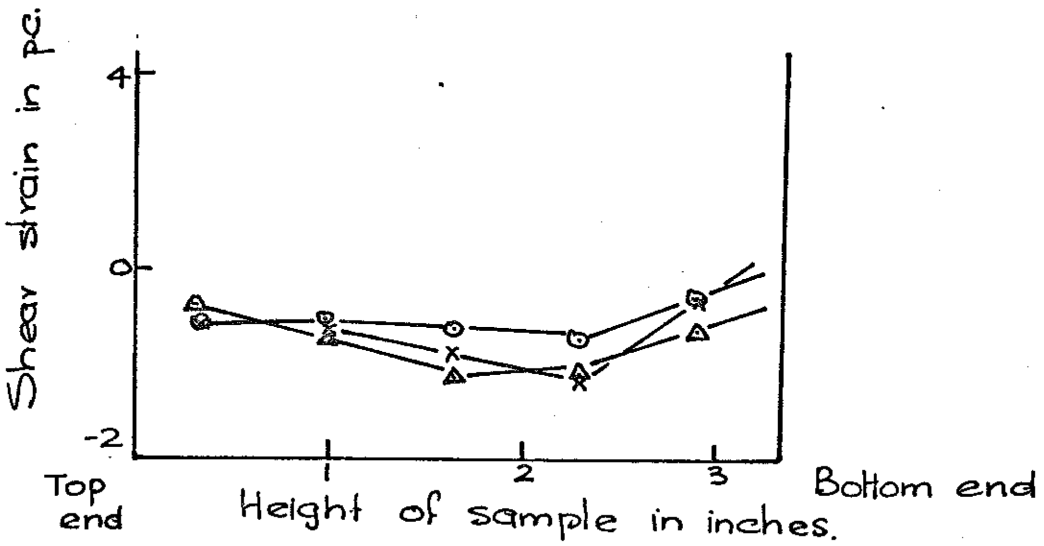

3.15 (d) Shear strain distribution.

Fig. 3.15 (a-d) Strain distributions plotted against height of sample during isotropic consolidation in a 1.5 inch diameter specimen contained between enlarged lubricated ends.

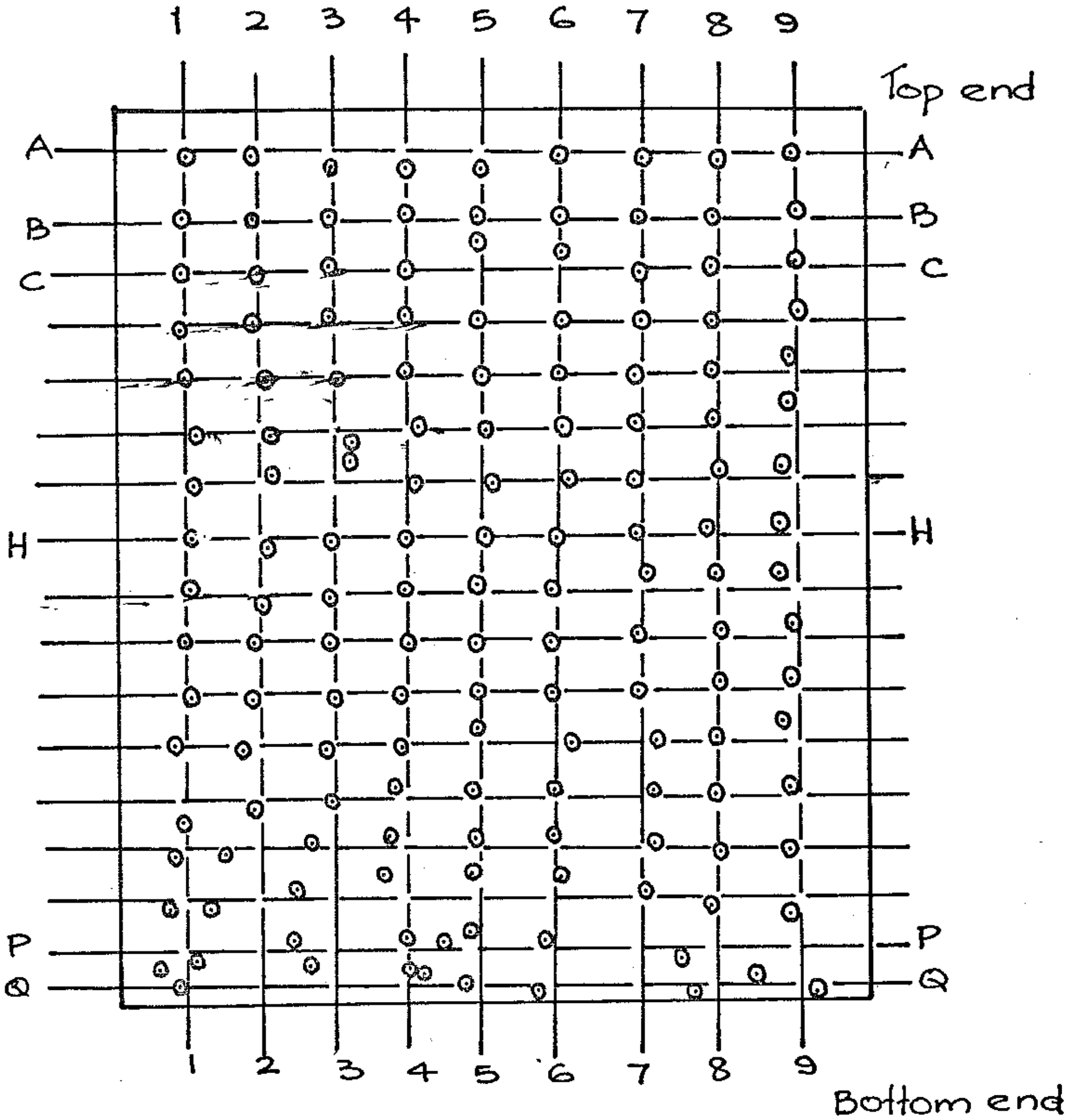

Fig. 3.16 (a) Positions of lead markers in plane 1 of sample OC

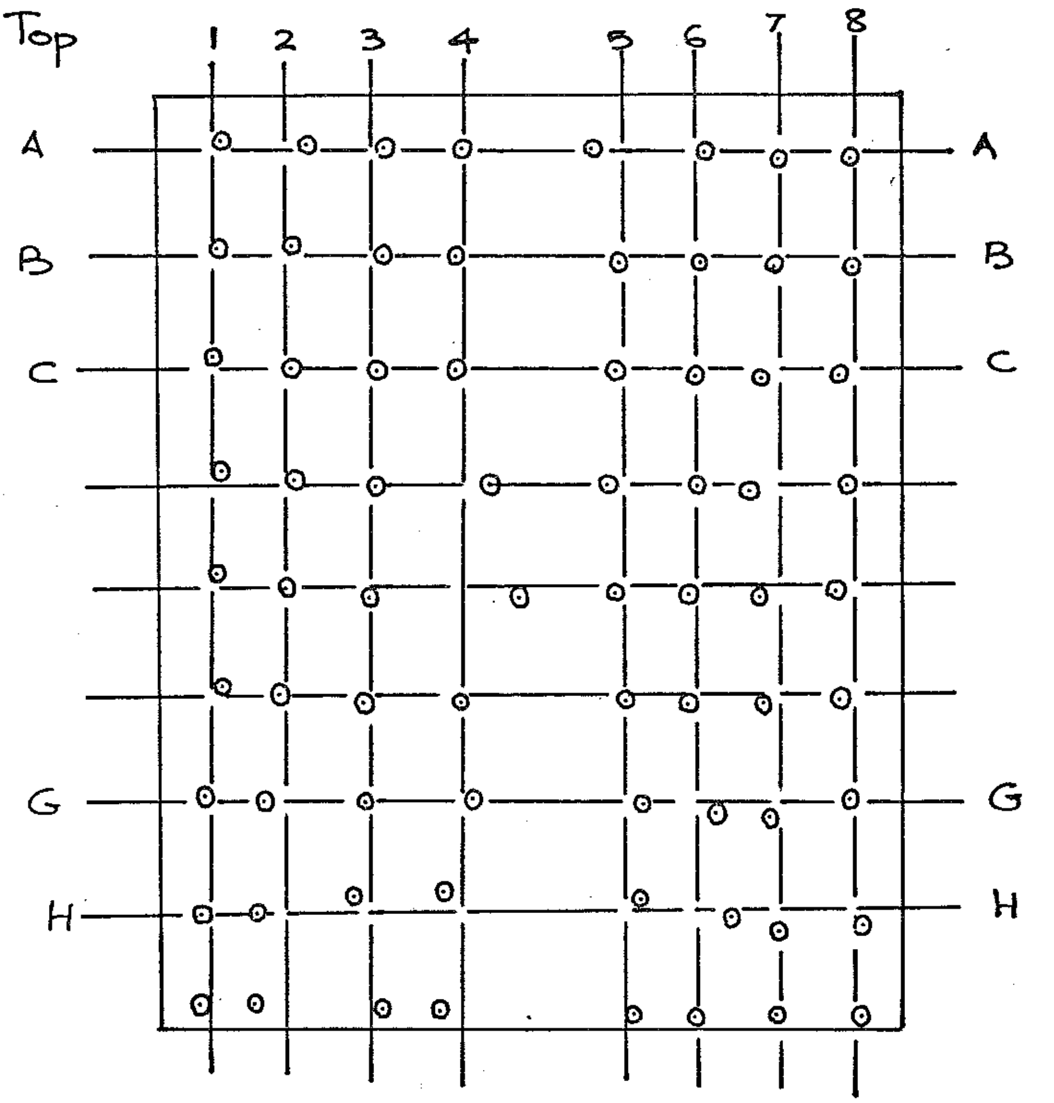

3.16(b) Positions of lead markers in plane 2 of sample OC